Interactive comment on "The Indian Summer Monsoon in MetUM-GOML2.0: Effects of air-sea coupling and resolution" *by* Simon C. Peatman and Nicholas P. Klingaman

Simon C. Peatman and Nicholas P. Klingaman

s.peatman@reading.ac.uk

It would be incorrect to refer to the coupling as "partial". In MetUM-GOML, the atmosphere-ocean coupler (OASIS) transfers the same information between atmosphere and ocean as it would in a model with ocean dynamics; the complexity of the ocean model has no bearing on the coupling. (It might be reasonable to refer to the blended grid boxes, indicated by $0 <$ weight < 1 in figure 1, as "partially coupled", because the atmosphere sees a weighted average of the ocean SST and a prescribed SST here, but certainly not for the weight $= 1$ regions.)

Although we do not make the change suggested by the reviewer, we emphasize that

the coupling is to a mixed layer ocean, without dynamics, wherever relevant (e.g., p4 l30; p7 l1; p7 l15; p8 ll1-2; p15 l2).

We thank the reviewer for the suggestion of adding indicators of statistical significance. Where the difference of two climatologies is plotted, a two-tailed Student's t-test on means is used ($H_0 : \mu_1 = \mu_2; H_1 : \mu_1 \neq \mu_2$) with $p = 0.01$. For precipitation, significance is indicated by stippling (figs 2b, 3a, 3b and 4) or (where wind vectors are also drawn so stippling would be in the way) insignificance by grey shading (figs 13a–c). For wind, vectors are shown only if at least one of u and v is significant (figs 2e, 3c, 3d and 13a–c). Where the ratio of two variances is plotted, a two-tailed f-test is used ($H_0 : \sigma_1^2 = \sigma_2^2; H_1 : \sigma_1^2 \neq \sigma_2^2$) with $p = 0.05$. Significance is indicated by stippling (figs 5b, 5d, 7b, 7c and 13d–f). These tests are also described in the main text (p5 ll20–24).

————————————————

Geosci. Model Dev. Discuss.,
https://doi.org/10.5194/gmd-2018-197-AC2, 2018

Interactive comment on "The Indian Summer Monsoon in MetUM-GOML2.0: Effects of air-sea coupling and resolution" *by* Simon C. Peatman and Nicholas P. Klingaman

Simon C. Peatman and Nicholas P. Klingaman

s.peatman@reading.ac.uk

We make clear in the text that certain aspects of the propagation are improved and others degraded when the ocean is coupled. The pattern correlation is one diagnostic we use, but we are clear that it does not tell the whole story. By splitting the propagation diagrams into three latitude bands (20°–2.5°S, 0°–10°N and 12.5°–40°N), we now see that by far the largest difference in pattern correlation comes from the first (southern hemisphere) band, with the globally-coupled experiment having by far the lowest correlation there. However, in the other bands, where most of the northward branch of the propagation occurs, the picture is more complex and the differences between experi-

ments are much smaller. For example, of the 90 km experiments listed in table 2, the experiment with coupling in only the Indian Ocean has the highest pattern correlation in the middle latitude band.

We rephrase the abstract (p1 ll8–9) to make it clear that some but not all aspects of propagation are improved by coupling, and clarify the relevant sentences in the main text also.

List of changes to manuscript

Old text in red replaced with *new text in green.*

Page 1, lines 8–9

However, coupling slightly improves the simulation of northward BSISO propagation over the Indian Ocean, Bay of Bengal and India.
Coupling slightly improves some aspects of the simulation of northward BSISO propagation over the Indian Ocean, Bay of Bengal and India, but degrades others.

Page 4, line 30

the effect of adding Indian Ocean coupling
the effect of adding Indian Ocean coupling to a mixed-layer ocean

Page 5, lines 20–24

Statistical significance tests are used when either comparing an experiment to observations or comparing one experiment to another. When comparing two sample means $\bar{x}_1$ and $\bar{x}_2$, significance is tested using a two-tailed t-test, with a null hypothesis $H_0 : \mu_1 = \mu_2$ and alternative hypothesis $H_1 : \mu_1 \neq \mu_2$, where μ is the population mean; when comparing two sample variances s_1^2 and s_2^2, significance is tested using a two-tailed f-test, with $H_0 : \sigma_1^2 = \sigma_2^2$ and $H_1 : \sigma_1^2 \neq \sigma_2^2$, where σ is the population variance (e.g., Riley et al., 2007).

Page 6, line 12

substantial biases throughout the domain
significant biases almost throughout the domain

Page 6, line 14

a substantial deficit
a significant deficit

Page 6, line 23

small biases in the mean low-level monsoon flow
small yet statistically significant biases in the mean low-level monsoon flow

Page 6, lines 27–28

much weaker but still evident northwesterly bias
much weaker but still significant northwesterly bias

Page 7, line 1

regional air-sea coupling
regional coupling to the mixed-layer ocean

Page 7, lines 6–7

coupling in any basin degrades the mean state
coupling in any basin significantly degrades the mean state

Page 7, line 15

the change in biases when coupling is introduced
the change in biases when coupling to the mixed-layer ocean is introduced

Page 7, line 29–33

u850 in GL$_{90}$ also exhibits excessive ISV (figure 5d; note the different colour scale) over much of the tropical west Pacific, except around the equator, but lacks variability over most of the Indian Ocean, especially around the equator where the northward-propagating events tend to originate. Again there is a lack of variability over India, especially in the west.

u850 in GL$_{90}$ also exhibits excessive ISV (figure 5d; note the different colour scale) over much of the tropical west Pacific, except around the equator. Although there is a lack of variability over most of the Indian Ocean, especially around the equator where the northward-propagating events tend to originate, it is not statistically significant. Again there is a lack of variability over India, especially in the west, which in some parts is statistically significant.

Page 8, lines 1–2

when adding or removing coupling
when adding or removing coupling to the mixed-layer ocean

Page 8, lines 26–29

suggesting that aspects of the propagation may be degraded by coupling, but the difference is minimal.
suggesting that some aspects of the propagation may be degraded by coupling. However, the difference is minimal and due almost entirely to the lack of southward propagation in the southern hemisphere, not to changes in the northward propagation. Indeed, the northward propagation just north of the equator is considerably stronger with Indian Ocean coupling (GL$_{90}$ and IO$_{90}$) than without it.

Page 8, lines 30–33

Despite the pattern correlations suggesting only minimal changes between these experiments with different coupling regions, there are some features which clearly do differ. In particular, the southward propagation is coherent only in GL$_{90}$, and the northward propagation from the equator to about 5°N is weak without Indian Ocean coupling (AO_PO$_{90}$).

Page 11, line 13

over India and the Indian Ocean
over India and the Indian Ocean (mainly in the northern hemisphere)

Page 11, lines 19–20

changes in mean precipitation are far smaller
changes in mean precipitation are generally insignificant

Page 11, line 29

still a major improvement
still a significant improvement

Page 11, line 30

almost no change
almost no significant change

Page 15, line 2

in the ISM
in the ISM using a mixed-layer ocean

Page 15, line 3

However, there is a slight improvement
However, there are slight improvements

Figure 2

Stippling indicates 99% statistical significance according to a two-tailed t-test.
...
vectors; shown only if statistically significant at the 99% level according to a two-tailed t-test

Figure 3

Stippling indicates 99% statistical significance according to a two-tailed t-test.

. . .

vectors (shown only if statistically significant at the 99% level according to a two-tailed t-test)

Figure 4

Stippling indicates 99% statistical significance according to a two-tailed t-test.

Figure 5

; stippling indicates 95% statistical significance according to a two-tailed f-test.

Figure 7

; stippling indicates 95% statistical significance according to a two-tailed f-test.

Figure 13

; grey shading indicates precipitation is statistically *insignificant* at the 99% level according to a two-tailed t-test; vectors (black) are shown only if statistically significant at the 99% level according to a two-tailed t-test.

. . .

; stippling indicates 99% statistical significance according to a two-tailed t-test.

The Indian Summer Monsoon in MetUM-GOML2.0: Effects of air-sea coupling and resolution

Simon C. Peatman[1] and Nicholas P. Klingaman[1]

[1]National Centre for Atmospheric Science–Climate and Department of Meteorology, University of Reading, UK

Correspondence: S. C. Peatman (s.peatman@reading.ac.uk)

Abstract. The fidelity of the simulated Indian Summer Monsoon is analysed in the UK Met Office Unified Model Global Ocean Mixed Layer configuration (MetUM-GOML2.0), in terms of its boreal summer mean state and propagation of the Boreal Summer IntraSeasonal Oscillation (BSISO). The model produces substantial biases in mean June–September precipitation, especially over India, in common with other MetUM configurations. Using a correction technique to constrain the mean seasonal cycle of ocean temperature and salinity, the effects of regional air-sea coupling and atmospheric horizontal resolution are investigated. Introducing coupling in the Indian Ocean degrades the atmospheric basic state, compared with prescribing the observed seasonal cycle of sea surface temperature (SST). This degradation of the mean state is attributable to small errors ($\pm 0.5°$C) in mean SST. ~~However, c~~Coupling slightly improves some aspects of the simulation of northward BSISO propagation over the Indian Ocean, Bay of Bengal and India, but degrades others. Increasing resolution from 200 km to 90 km grid spacing (approximate value at the equator) improves the atmospheric mean state, but increasing resolution again to 40 km offers no substantial improvement. The improvement to intraseasonal propagation at finer resolution is similar to that due to coupling.

Copyright statement. TEXT

1   Introduction

The Indian Summer Monsoon (ISM) is one of the most significant features of the tropical climate, with boreal summer (June to September; JJAS) rains bringing around 80% of the annual precipitation over much of India. Mainly through its effect on agriculture, the monsoon affects the livelihoods of over one billion people. The total summer rainfall over the monsoon region is remarkably consistent year-to-year, with interannual variability (IAV) of only around 10% of the mean (Turner and Annamalai, 2012), but the most extreme years still have significant impacts on Indian foodgrain production and gross domestic product, especially in years of rainfall deficit (Gadgil and Gadgil, 2006). However, even years in which the all-India rainfall is around normal can see dramatic impacts on agriculture at a local level due to the IAV of rainfall distribution. Further variations include IAV in the onset and withdrawal dates of the monsoon, and intraseasonal active-break cycles within a monsoon season. Accurate forecasting of such IAV and intraseasonal variability (ISV) is, therefore, of crucial socio-economic importance to the region.

ISV in the monsoon over the Bay of Bengal (BoB) was arguably first recorded by Halley (1686) following wind reports from British navigators. In describing the boreal summer monsoon he noted that "the Winds are not so constant, either in strength or point [direction], in the Gulph of Bengall [BoB], as they are in the Indian-Sea [Arabian Sea], where a certain steady Gale scarce ever fails". In the satellite era the leading mode of ISV was shown to involve the northward propagation of convection over the monsoon region with period of 40–50 days (e.g., Yasunari, 1979), associated with the monsoon active-break cycle the eastward-propagating Madden-Julian Oscillation (MJO). Eastward MJO propagation occurs in all seasons, although it is strongest in boreal winter (Wheeler and Hendon, 2004), while northward propagation is observed only in boreal summer (e.g., Lau and Chan, 1986). Lee et al. (2013) developed indices for two modes of the boreal summer intraseasonal oscillation (BSISO) based on multivariate empirical orthogonal function (MV-EOF) analysis of outgoing longwave radiation (OLR) and zonal wind at 850 hPa ($u850$). The first mode (BSISO1) propagates northward with a "quasi-oscillating" period of 30–60 days, while the second mode (BSISO2) propagates northward/north-westward with period of 10–30 days and is prominent from late April through to June (the pre-monsoon and monsoon onset periods).

Numerous studies have considered the ability of general circulation models (GCMs) to simulate the monsoon and its associated ISV. A model intercomparison study by Waliser et al. (2003), using ten atmosphere-only models (AGCMs), found that many AGCMs have ISV in boreal summer, with some overestimating and others underestimating its amplitude, and generally capture some northward propagation. Fang et al. (2017) showed that the atmosphere-only Met Office Unified Model (MetUM; using the Global Atmosphere 3.0 (GA3) configuration) simulated the northward propagation well, especially when increasing the resolution from a grid spacing of 200 km to 90 km (at the equator). An increase in resolution in MetUM-GA3 – up to a 40 km grid spacing at the equator – slightly improved JJAS mean state precipitation biases and the representation of monsoon depressions, although substantial systematic errors remained (Johnson et al., 2016).

Fu and Wang (2004) compared the performances of atmosphere-only and coupled configurations of the European Centre for Medium-Range Weather Forecasts–Hamburg GCM version 4 (ECHAM4) to investigate the effect of coupling in the BSISO. To ensure a similar basic state in each model, the daily mean sea surface temperature (SST) from the coupled model run was used to force the atmosphere-only model (with small noise perturbations applied). Coupling significantly improved the strength of the northward part of the BSISO and the phase relationship between SST and convective precipitation. Klingaman et al. (2008) showed that daily SST forcing in an AGCM gives stronger variability in the BSISO than monthly SST, although the high-frequency forcing strengthened an incorrect in-phase relationship between convection and SST. DeMott et al. (2015) subsequently concluded that AGCMs should not be forced with such high-frequency SSTs for studies of tropical ISV, as this can produce apparently-better ISV due to erroneous positive feedbacks from incorrect relationships between SST, surface fluxes and convection. DeMott et al. (2011, 2014) found that the coupled Community Climate System Model also produced a more realistic intraseasonal oscillation its counterpart AGCM, consistent with Fu and Wang (2004). Specifically, DeMott et al. (2011) found that the coupling improved the mean state in the BSISO domain, reduced excess tropical variability and improved the phase relationship between SST and convection.

Overviews of the ability of state-of-the-art coupled GCMs to simulate the monsoon were presented by Lin et al. (2008) and Sperber et al. (2013). The former study evaluated the representation of ISV in the monsoon in Coupled Model Intercomparison

Project phase 3 (CMIP3) models, while the latter compared models from CMIP3 and CMIP5. The mean precipitation in the ISM region is simulated well by CMIP3 models but there is a general lack of ISV, including in the BSISO. Only four or five of the 14 models studied had a spectral peak in the frequency band relating to BSISO variability. In terms of the multi-model mean (MMM), CMIP5 models produce a more realistic monsoon than those from CMIP3, but significant biases remain. The

5 JJAS mean precipitation exhibits a dry bias over most of India in the MMM from each of the two CMIPs, of up to 4 mm day^{-1}. While the CMIP3 MMM failed to capture the region of enhanced precipitation over the Western Ghats, in the CMIP5 MMM this feature was present but its the magnitude was still too low. Both the CMIP3 and CMIP5 MMMs had wet biases of around 2–3 mm day^{-1} over the north-west Indian Ocean and the Maritime Continent (except Borneo, where the bias is around zero). CMIP5 showed a clear improvement over CMIP3 in terms of increased 20–100-day filtered OLR variance over India and the

10 Indian Ocean, including the BoB, but the Indian Ocean variance – in the region of the canonical northward propagation – was still too low.

The present study uses the Global Ocean Mixed Layer coupled configuration of the Met Office Unified Model (MetUM-GOML2.0; Hirons et al., 2015), comprising the MetUM Global Atmosphere 6.0 (GA6; Walters et al., 2017) coupled to the Multi-Column K Profile Parameterisation ocean (MC-KPP, version 1.1).

15 MC-KPP consists of independent one-dimensional columns – one under each atmospheric grid box – which simulate vertical mixing using the scheme of Large et al. (1994), but not horizontal or vertical advection. Each column is forced at the surface every three hours with heat, fresh water and momentum fluxes. This setup is considerably computationally cheaper than a fully coupled model (i.e., an atmosphere model coupled to an ocean model with full dynamics) whilst still providing air-sea interactions. MetUM-GOML2.0 also has the advantage that, due to the ocean columns being independent, individual columns

20 may be switched on and off in space and/or time, with SST prescribed where the columns are switched off. This makes the model a powerful tool for investigating the effect of coupling in, for example, particular ocean basins. Furthermore, the ocean mean state may be constrained through a correction technique to produce a model mean state with smaller biases than in a fully coupled GCM (see section 2.1).

The use of this model is motivated by questions concerning the role of air-sea interactions in the monsoon ISV, specifically

25 the BSISO. For example, the relative effects of local and remote air-sea interactions are not well understood, so the ability to couple the atmosphere and ocean regionally is of great importance. Furthermore, we wish to investigate these effects in a model with a near-observed ocean mean state, to avoid the considerable ocean biases in a fully coupled model which can degrade ISV (e.g., Klingaman and Woolnough, 2014b). We also wish to investigate the effect of resolution in a coupled model with a consistent mean state across resolutions.

30 Klingaman et al. (2011) coupled an earlier MetUM version – the Hadley Centre Atmospheric Model version 3 (HadAM3) – to the KPP ocean and tested a range of coupling frequencies and vertical resolutions for the ocean mixed layer. The highest vertical resolution and coupling frequency (1 m, every 3 hours) produced a northward-propagating BSISO similar to observations, while the coarsest resolution and lowest frequency (10 m, every 24 hours) had much weaker propagation and only around 60% of the observed ISV in both SST and precipitation. Hirons et al. (2015) showed that coupling in MetUM-GOML1

35 improves known MetUM biases, including the equatorial Indian Ocean wet bias (Ringer et al., 2006; Sperber et al., 2013) and

the amplitude of tropical ISV of convection, especially in the MJO. However, these improvements did not remove these biases completely, and there was almost no impact on the significant lack of precipitation in the MetUM over India during JJAS.

Section 2 of this paper describes the setup of the MetUM-GOML2.0 experiments, as well as the data sets and methods used. Results are presented in section 3, and discussed and summarized in section 4.

2 Methodology

2.1 Model setup

In this study we examine a series of MetUM-GOML2.0 integrations. Note that the version of the model described by Hirons et al. (2015) was MetUM-GOML1. The only changes in version 2.0 are updating the atmosphere from the MetUM GA3 to GA6 and the mixed layer ocean from MC-KPP version 1.0 to 1.1 (the only change here being a new coupling scheme, required for GA6).

We employ an ocean correction technique, as described in detail in section 2.1.1 of Hirons et al. (2015). This allows us to constrain the mean seasonal cycle of temperature and salinity throughout the ocean column. First, a 10-year relaxation run is performed, relaxing with a 15-day timescale towards an observed seasonal cycle of ocean temperature and salinity computed from 1980–2009 (Smith and Murphy (2007); hereafter SM07) and interpolated to daily means using the Atmospheric Model Intercomparison Project (AMIP) II method (Taylor et al., 2000). The mean seasonal cycle of the temperature and salinity relaxation increments is then computed. Physically, these increments account for the effects of ocean advection and of biases in the atmospheric surface fluxes. The seasonal cycle of these increments is applied in a subsequent integration to constrain the basic state temperature and salinity. This integration is analysed. These integrations were run for 28 years each, unless otherwise stated. This technique is used for all coupled simulations in this paper, with separate flux corrections computed for each.

Coupling in MetUM-GOML2.0 always excludes regions in which a certain threshold of sea ice is exceeded in the AMIP data set used in the CMIP5 (Taylor et al., 2012), since the MC-KPP model does not simulate sea ice. (Details may be found in section 2.2 of Hirons et al. (2015).) Where there is no coupling the mean seasonal cycle of SST from SM07 is prescribed. Between the regions of coupling and no coupling a blending region of around $10°$ width smooths any discontinuities. In this blending region the SST returned to the atmosphere is a weighted average of the MC-KPP value and the prescribed SM07 value.

A climate integration (GL_{90}) was run at N216 resolution (approximately 90 km grid spacing at the equator) with near-global coupling to MC-KPP as shown in figure 1a. Several sensitivity experiments were then performed (table 1). In AO_PO_{90}, coupling is switched off in the Indian Ocean and left on in the Atlantic and Pacific Oceans (figure 1b), so the difference between GL_{90} and AO_PO_{90} quantifies the effect of adding Indian Ocean coupling to a mixed-layer ocean (when Atlantic and Pacific Ocean coupling are present). In the uncoupled region, the mean seasonal cycle of SST from SM07 is prescribed. Similarly, IO_{90} has coupling in the Indian Ocean only (figure 1c).

To investigate the effects of coupling, atmosphere-only (MetUM-GA6) experiments were performed using the SST from GL$_{90}$, so that these experiments have the same SST biases as GL$_{90}$. In ATM$_{90}$[G̃L] the GL$_{90}$ SST was 31-day smoothed, removing much of the ISV; and in ATM$_{90}$[$\overline{\mathrm{GL}}$] the mean seasonal cycle from GL$_{90}$ was used every year so that the simulation had no IAV of SST. Similarly, ATM$_{90}$[ĨO] uses 31-day smoothed SST from IO$_{90}$. As mentioned in section 1, DeMott et al. (2015) showed that forcing an atmosphere-only model with high-frequency (e.g., daily) SST from a coupled simulation is inadvisable because it may produce realistic-looking ISV for spurious reasons, hence the decision to apply a 31-day smoothing here.

Finally, the effect of atmospheric horizontal resolution was investigated using experiments with coupling in the Indian Ocean only, using resolutions N96 (IO$_{200}$, run for 29 years) and N512 (IO$_{40}$, run for 15 years), where subscripts again denote approximate grid spacings at the equator in km. An advantage of using MetUM-GOML2.0 for this resolution comparison is that we can ensure the SST mean state is consistent at each resolution whilst retaining air-sea coupling.

2.2 Data sets

The following data sets are compared against model output and, in the case of OLR and $u850$, used to compute of the BSISO MV-EOFs following Lee et al. (2013). Daily mean precipitation is from the Global Precipitation Climatology Project (GPCP; Huffman et al., 2001) at 1° resolution for 1997–2014. Daily mean winds and SST are taken from the European Centre for Medium-Range Weather Forecasts Interim Reanalysis (ERA-Interim; Dee et al., 2011) for 1982–2010. Daily mean OLR observations are taken from the Advanced Very High Resolution Radiometer (AVHRR) at 2.5° resolution for 1981–2010.

2.3 Data analysis methods

To investigate ISV (section 3.2) we use a Lanczos bandpass filter (Duchon, 1979) with frequency cut-offs of 1/70 and 1/24 cycles per day (cpd) and order 120 (i.e., 241 weights).

Statistical significance tests are used when either comparing an experiment to observations or comparing one experiment to another. When comparing two sample means $\bar{x}_1$ and $\bar{x}_2$, significance is tested using a two-tailed t-test, with a null hypothesis $H_0 : \mu_1 = \mu_2$ and alternative hypothesis $H_1 : \mu_1 \neq \mu_2$, where μ is the population mean; when comparing two sample variances s_1^2 and s_2^2, significance is tested using a two-tailed f-test, with $H_0 : \sigma_1^2 = \sigma_2^2$ and $H_1 : \sigma_1^2 \neq \sigma_2^2$, where σ is the population variance (e.g., Riley et al., 2007).

The northward BSISO propagation is diagnosed using lag correlations of data, filtered as above. Data (e.g., OLR) from May to October are selected from the filtered time series. Lag correlations are then computed, using the method of Trenberth (1984), between the 70°–100°E mean and the time series at 85°E, 12.5°N. This is performed at every latitude from 20°S to 40°N for lags up to ±20 days. This is also performed with SST averaged over 70°–100°E and OLR at 85°E, 12.5°N, to show the phase relationship between SST and OLR. SST correlations are calculated up to 17.5°N only, since northwards of this point the majority of the zonal extent of the domain is land.

We further investigate monsoon ISV using the BSISO analysis of Lee et al. (2013) (section 3.3). MV-EOF analysis of OLR and $u850$ is used to define eight phases for each of the leading two modes of the BSISO. OLR and $u850$ – with the climatology, first three harmonics of the annual cycle and a 120-day running mean removed – are used for the domain 10°S–

40°N, 40°–160°E and for May to October only. The two fields are normalized by their respective area-mean standard deviation and the leading four MV-EOFs are computed. The OLR and $u850$ data are projected onto these EOFs to find the four leading principal component (PC) time series, which are each normalized by their standard deviation. On any given day the location in normalized (PC2, −PC1) space defines the amplitude and phase of BSISO1, and similarly with (PC4, −PC3) space for BSISO2.[1]

3 Results

3.1 Model mean state

We first examine the JJAS mean state. In GPCP (figure 2a) an average of 4–7 mm day^{-1} falls over most of India, with the heaviest rainfall over the north-east BoB, where the average exceeds 11 mm day^{-1} and is more than 15 mm day^{-1} in a narrow band parallel to and adjacent to the coast of eastern Bangladesh and northern Myanmar. (A version of this figure was also produced using the monthly mean GPCP data for 1982–2010 (not shown) as this has a much longer data record, but there were no substantial differences.) GL$_{90}$ has ~~substantial~~significant biases almost throughout the domain (figure 2b). Over India the daily mean rainfall deficit exceeds 4 mm day^{-1} in almost all places; over much of the region this equates to a deficit of over 70% (figure 2c). Over the BoB there is a ~~substantial~~significant deficit in the west, but rainfall is close to the GPCP value or even slightly higher in the east. The Indian Ocean sees two distinct regions between 55° and 100°E, with a strong wet bias north of the equator and dry bias to the south. Similarly, over the South China Sea and western tropical north Pacific there is a strong wet bias whereas to the south, within the Maritime Continent, there is a dry bias (especially over the sea).

These are long-standing biases across many MetUM configurations. For example, in the coupled Hadley Centre Global Environmental Model HadGEM2-AO and in MetUM-GC2 (Williams et al., 2015) the signs of the boreal summer precipitation biases are the same as above. Atmosphere-only experiments with GA3 (Johnson et al., 2016) and GA6 (Walters et al., 2017) show similar biases, although there was no dry bias just south of the equator in the Indian Ocean and there was a dry bias in the South China Sea.

Over the Indian Ocean GL$_{90}$ has only small yet statistically significant biases in the mean low-level monsoon flow (figure 2d,e), with slightly too strong southerlies south of the equator at 75–100°E and a very slightly too weak jet east of the Horn of Africa. However, it may be that the wind field is quite unrealistic for the given precipitation field. Larger wind biases exist over India, where the flow should be westerly; to the north there is strong southwesterly bias, with anomalous flow from the Arabian Sea towards the Himalayas; and to the south there is a much weaker but still ~~evident~~significant northwesterly bias. Thus the monsoon flow is bifurcated as it reaches the land, albeit with a much stronger branch to the north than to the south, which is consistent with the dry bias over the country. When the monsoon jet reaches Indochina the strong westerlies erroneously extend into the Pacific Ocean, between 5° and 20°N, to the extent that it weakens the easterly flow over the tropical Pacific Ocean.

---

[1] The ordering and sign of the PCs appears to have been chosen for consistency with the pre-existing RMM indices for the MJO, and bearing in mind the sign convention already adopted for EOFs 1 and 3.

To investigate the effect of regional ~~air-sea~~ coupling to the mixed-layer ocean we compare GL_{90} to AO_PO_{90} (figures 3a,c), and to IO_{90} (figures 3b,d; see table 1). Adding Indian Ocean coupling has very little effect over land, but a substantial impact on biases over ocean (figures 3a,c). Indian Ocean coupling reverses the sign of the mean rainfall bias south of the equator, but increases the wet bias north of the equator and in the Pacific Ocean. The strong jet extending from the BoB to the west Pacific

5   exists in AO_PO_{90} and is worsened by Indian Ocean coupling. The effect of Atlantic and Pacific Ocean coupling is similar (figures 3b,d) in both precipitation and wind, but with more impact over the Pacific than Indian Ocean. Thus, coupling in any basin significantly degrades the mean state over both the Indian and Pacific Oceans, but most significantly over the basin in which coupling is introduced.

Coupling introduces IAV and ISV in SST, as well as errors in the mean SST. (Although the mean state was constrained

10   through applying corrections to the ocean, there are SST biases on the order $\pm0.5°C$ in the Indian Ocean; see figure 4.) Any or all of these effects could produce the differences seen in figure 3. To separate these effects we consider two further experiments: $ATM_{90}[\tilde{GL}]$, with prescribed SST from GL_{90} with a 31-day smoothing applied to remove much of the SST ISV; and $ATM_{90}[\overline{GL}]$, with prescribed SST from the mean seasonal cycle taken from GL_{90} to remove SST IAV and ISV. There are no substantial differences in mean precipitation or 850 hPa wind between GL_{90} and either of these runs (not shown). Therefore,

15   the change in biases when coupling to the mixed-layer ocean is introduced cannot be attributed directly to the introduction of feedbacks at the surface, nor to the ISV or IAV introduced into the ocean. Since SSTs in $ATM_{90}[\tilde{GL}]$ and $ATM_{90}[\overline{GL}]$ are taken from GL_{90}, the mean state biases are the approximately the same in the Indian Ocean in all three experiments. Having eliminated other possibilities, it follows that the change in atmospheric biases when coupling is introduced is attributable to these SST biases.

20 **3.2   Intraseasonal variability**

We now investigate ISV using filtered data as described in section 2.3, for GPCP precipitation and ERA-Interim $u850$ (figures 5a,c). In both fields there is significant ISV over the Indian Ocean – both over the equator and further north in the BoB – as well as over India and the tropical west Pacific. The relative lack of ISV over the Maritime Continent region is consistent with the weak MJO in boreal summer.

25   Over ocean the ISV of precipitation in GL_{90} is slightly too high, especially in the west Indian and west Pacific Oceans (figure 5b). Notably, however, ISV over the BoB is very similar to observed. The most significant bias is a severe lack of variability (less than a tenth of the observed amount) over the Indian states of Gujarat and Rajasthan, Pakistan, Afghanistan, and the north-east Arabian Sea. The rainfall deficit is over 90% in the same region (figure 2c), suggesting that in the model the monsoon onset does not reach this area or the monsoon is in near-permanent break conditions. $u850$ in GL_{90} also exhibits

30   excessive ISV (figure 5d; note the different colour scale) over much of the tropical west Pacific, except around the equator~~., but lacks~~ Although there is a lack of variability over most of the Indian Ocean, especially around the equator where the northward-propagating events tend to originate, it is not statistically significant. Again there is a lack of variability over India, especially in the west, which in some parts is statistically significant.

In section 3.1 (figure 3a–c) the changes in the model mean state bias when adding or removing coupling to the mixed-layer ocean were attributed to changes in mean SST. A similar conclusion can be drawn in the case of biases in ISV as over ocean there is almost no difference in ISV amplitude between GL_{90} and $ATM_{90}[\tilde{GL}]$ or $ATM_{90}[\overline{GL}]$ (not shown).

As mentioned in section 1, the canonical view of summer ISV in the region in question is northward propagation of convection, originating around the equatorial Indian Ocean and propagating northwards over India and the BoB. This propagation is investigated in figure 6, which shows lag correlations calculated as described in section 2.3. Lag correlation of OLR is shown in the coloured shading. Propagation speed is estimated by joining the points of maximum lag correlation at $0°$, $12.5°$ and $20°N$ with straight line segments. These speeds are listed in table 2 along with the pattern correlation against observations for each experiment. Lag correlation of SST against OLR at the basepoint is shown in the black contours, with solid contours indicating a negative correlation (i.e., warm SST associated with active convection).

The observations (figure 6a) show convection originating just south of the equator and propagating northwards, reaching $12.5°N$ about 11 days later before dying out between $20°$ and $30°N$. The propagation doubles in speed from 1.61 to 3.22 m s^{-1} once it reaches the BoB. There is also a southward branch, also originating from near the equator and propagating more quickly than its northward counterpart but dying out sooner, after about 5 days between $10°$ and $20°S$. The propagation is preceeded and followed by a region of opposite-signed OLR anomalies such that the oscillation has a period of around 36 days.

In GL_{90} (figure 6b) propagation is weaker or less coherent than observed, and the origin of the propagating convection lies too far north (on the equator). The pattern correlation between GL_{90} and observations is 0.838 (see table 2); this metric will also be used to compare experiments, below. The propagation to $12.5°N$ is at the correct speed but fails to increase thereafter. The southward branch is present but is considerably weaker and slower than observed. The time lag between opposite phases is approximately 16 days, giving a period of 32 days, slightly shorter than observed.

Figure 6a shows that SST and OLR are in quadrature, with positive SST anomalies leading active convection by about 9 days or a quarter-phase. This is consistent with previous observations of both the BSISO and the MJO (e.g., Hendon and Glick, 1997; Fu and Wang, 2004; Yang et al., 2008). This phase relationship is simulated well in GL_{90}.

The effect of regional coupling is again investigated in AO_PO_{90} and IO_{90} (figures 6c,e). In both experiments the northward propagation remains and the pattern correlation with observations is slightly higher than for GL_{90} (0.869 for AO_PO_{90} and 0.893 for IO_{90}), suggesting that some aspects of the propagation may be degraded by coupling. However, ~~but~~ the difference is minimal and due almost entirely to the lack of southward propagation in the southern hemisphere, not to changes in the northward propagation. Indeed, the northward propagation just north of the equator is considerably stronger with Indian Ocean coupling (GL_{90} and IO_{90}) than without it. All three experiments considered so far have too slow a phase speed, but IO_{90} is closest to observations and has an 80% increase in speed north of $12.5°N$. ~~Despite the pattern correlations suggesting only minimal changes between these experiments with different coupling regions, there are some features which clearly do differ. In particular, the southward propagation is coherent only in GL_{90}, and the northward propagation from the equator to about $5°N$ is weak without Indian Ocean coupling (AO_PO_{90}).~~

In both $ATM_{90}[\tilde{GL}]$ and $ATM_{90}[\tilde{IO}]$ the northward propagation remains but is slightly weaker than in their respective coupled experiments, especially between the equator and about $5–10°N$. However, in each case the southward branch of the propagation

is (even) weaker than in the coupled experiment. $\text{ATM}_{90}[\tilde{\text{GL}}]$ has less than 10% of the SST ISV found in ERA-Interim in the Indian Ocean (figure 7c; similarly for $\text{ATM}_{90}[\tilde{\text{IO}}]$ (not shown)). Hence, the ISV in SST provided by coupling is most beneficial to the simulation of ISV of convection in the region of the equator, and is less important northwards of around $10°$N. Removing IAV of SST in $\text{ATM}_{90}[\overline{\text{GL}}]$ slightly strengthens propagation in the equatorial region, although it does substantially slow propagation north of $12.5°$N, which was already too slow in GL_{90}. The impact of SST IAV, which in this model is mostly noise, is a surprising result which we have not been able to explain.

In the experiments with no Indian Ocean coupling (AO_PO_{90}, $\text{ATM}_{90}[\tilde{\text{GL}}]$, $\text{ATM}_{90}[\overline{\text{GL}}]$ and $\text{ATM}_{90}[\tilde{\text{IO}}]$) the phase relationship between SST and convection breaks down absolutely. There is no ISV of SST here, yet the convection is able to propagate. This is contrary to Klingaman et al. (2008), who found that HadAM3 produced almost no propagation with monthly mean SST but strong propagation with daily mean SST forcing.

3.3   BSISO indices

The MV-EOFs of OLR and $u850$ used for the BSISO indices were computed using the method of Lee et al. (2013) (see section 2.3) from GL_{90}, and are shown in figure 8e–h. These were also computed from observed OLR and reanalysis $u850$ (figures 8a–d). For consistency with earlier figures, we take the wind from ERA-Interim. The meridional component of the 850 hPa wind was computed by regression onto the respective PCs to show a full wind field. The leading two GL_{90} EOFs have a broadly similar structure, at the large scale, to those in observations although they explain a smaller fraction of the variance (7.8% and 4.7% respectively for GL_{90}, compared with 8.4% and 5.4% for observations). However, while EOF3 from GL_{90} has a broadly similar structure to observed EOF4, EOF4 from GL_{90} does not resemble any of the leading four observed EOFs. Therefore, to use the model EOFs to define a simulated BSISO2 would be inconsistent with the observed intraseasonal oscillation.

The same analysis was performed with the other model experiments described here (not shown). As in GL_{90}, some EOFs broadly match the observations but not always in the correct order, while others do not resemble any of the leading four observed EOFs. Furthermore, the EOFs are not consistent between experiments. Therefore, in the following we project model output onto the EOFs calculated by Lee et al. (2013), which used the NCEP/Department of Energy (DOE) Reanalysis II for the wind but are otherwise the same as figures 8a–d.

Figure 9 shows the mean annual cycle of variance of each of the leading four pseudo-PCs from observations/ERA-Interim and GL_{90}. (These are pseudo-PCs because the data being projected is not the same as was used to generate the EOFs, but hereafter are referred to as PCs for brevity.) In observations the variance of PCs 1 and 2 has a broad peak throughout boreal summer (May onwards), tailing off gradually from October onwards. In GL_{90} they decrease rapidly during August to a minimum in September, before increasing again slightly to a secondary maximum in October. Otherwise, the annual cycle is very similar to observations. The annual cycle of PC3 also shows a broad peak in boreal summer in GL_{90} and is roughly similar to the cycle of PC4 in observations, which is consistent with GL_{90} EOF3 resembling observed EOF4. In observations PC3 has most of its variance in the pre-monsoon and monsoon onset period but this is not seen in the remaining GL_{90} PCs. Similar behaviour is seen in other experiments (not shown), suggesting that BSISO1 is simulated reasonably well in MetUM-GOML2.0 (except

during September when it is less active) but that the model does not associate BSISO2 with the correct part of the monsoon cycle.

Composites of daily mean precipitation and 850 hPa wind are shown in figure 10 as anomalies from climatology, using May–October data only. Days are included in the composite only if the BSISO1 amplitude $\sqrt{\text{PC1}^2 + \text{PC2}^2}$ is at least 1.5. Both show the same broad structure (as they must by construction, since the OLR and $u850$ must project reasonably strongly onto the MV-EOFs for a day to contribute to the composite). However, there is a substantial difference over India, where the precipitation anomaly is almost always near-zero in the model, especially in the west. We have already seen (figures 2b,c) that there is very little rainfall over this area, so there could never be a substantial negative anomaly here (since precipitation is positive-definite), but we now see that there is also no significant positive anomaly at any point in the intraseasonal cycle. Indeed, the only region in which the BSISO1 pattern breaks down in the model is over India and, in some phases, the Indian Ocean (e.g., phase 8). The relationship between convection and circulation is fairly realistic, even over India and the Arabian Sea, despite the convective anomalies being weak. Lag correlations (figure 11) show that the wind lags the precipitation by 6–10 days (observations) or 2–5 days (GL$_{90}$). Thus, on intraseasonal timescales, the circulation may respond to convection but not the other way round.

To investigate propagation within BSISO1, instances of propagation from one phase to the next (e.g., 4 to 5, or 8 to 1) were found in the time series of phases, with the phase having been replaced with a 0 on days when the BSISO1 amplitude was below 1.5 (i.e., was inside the centre circle in figure 12a; where PC1 and PC2 were normalized to unit variance). Such propagation events were then classified by their length. For example, a propagation event through phases 6,7,8,1 has length 4, where BSISO1 may have stayed in each of the given phases for multiple days, provided there were no days breaking the sequence. In 30 years of observations from 1981 to 2010 there were 36 events of length 3 or more (1.2 yr^{-1}), with the longest spanning 6 phases. (In comparison, for the MJO it is not uncommon to have events of length 10 or more (Peatman et al., 2015).) In all experiments the frequency of such events was 1.0–1.3 yr^{-1}, except ATM$_{90}$[$\tilde{\text{GL}}$] which had only 0.8 yr^{-1}. Simulated events were most likely to be initiated in phase 5, which agrees with observations. Thus, BSISO1 propagation is broadly realistic, with little substantial difference between the experiments.

Composites of BSISO1 propagation events were computed by selecting all days on which the BSISO1 amplitude exceeded 1.5. These days were all defined as the start of an event and binned according to the BSISO1 phase on that date, with phases paired together: phases 8 & 1, phases 2 & 3, phases 4 & 5, and, phases 6 & 7. Composites were calculated by averaging over 15-day time series of the PCs, beginning on each of the selected days, separately for each pairs of start phases. The amplitude was then calculated for each day, and the resulting time series are plotted in figure 12b–e as a fraction A/A_1 of the amplitude on the first day. This indicates how rapidly the BSISO1 events decay. The horizontal line on each panel is $1.5/A_1$ for observations, showing the point at which the observed composite decays into the centre circle.

Observed BSISO1 events decay quite rapidly, generally reaching $A = 1.5$ in 3–4 days. Generally speaking, the model composites beginning in phases 4–5 (when active convection is over India and the Maritime Continent) decay too rapidly, and those beginning in phases 2–3 (active over the Indian Ocean and east Asia) and 6–7 (active over the BoB and South China Sea) decay too slowly. GL$_{90}$ is reasonably realistic in its propagation as the curves shown are closest to the observations, the major

exception being for events beginning in phases 6 and 7. As found in figure 6, however, there is little consistency between the other experiments as to which performed more realistically. Hence, when BSISO1 becomes strong, the statistics of subsequent propagation are fairly realistic, and not systematically dependent on SST biases and variability.

It is notable that there is a fairly realistic representation of the BSISO in MetUM-GOML2.0, even though the model's mean state precipitation is particularly poor. Therefore, a model's ability to simulate boreal summer ISV, and in particular the northward propagation of convection, clearly does not depend on the mean state precipitation.

3.4 Effect of resolution

We now consider the effect of horizontal resolution on the simulation of the ISM in MetUM-GOML2.0, in simulations with Indian Ocean coupling (IO_{200}, IO_{90} and IO_{40}). We first consider the effect on the mean state and then the effect on ISV, including the BSISO1 indices.

GL_{90} and IO_{90} have almost exactly the same pattern in the sign of rainfall and 850 hPa wind biases but with some differences in magnitude (figures 3b,d). Increasing the resolution from IO_{200} to IO_{90} (figure 13b) slightly improves the mean state precipitation over India and the Indian Ocean (mainly in the northern hemisphere). Indian rainfall increases by up to 2 mm day^{-1}, although this is much smaller in magnitude than the dry bias of up to 6 mm day^{-1} in IO_{90}. Similarly, just north of the equator in the Indian Ocean there is a wet bias in IO_{90} of over 10 mm day^{-1} at its peak, which is at most 4 mm day^{-1} drier than in IO_{200}. Over the BoB the increase in precipitation from IO_{200} to IO_{90} is roughly half the magnitude of the dry bias in IO_{200} (not shown). The greatest change resulting from this increase in resolution, however, is in the Pacific Ocean, where there is no coupling. There is a substantial decrease in precipitation and weakening of the westerly jet extending over the same region, approximately halving the magnitude of the IO_{200} biases. As the resolution increases from IO_{90} to IO_{40} (figure 13c) the changes in mean precipitation are ~~far smaller~~generally insignificant, with some minimal decreases in the bias over ocean and almost no change over land.

The changes in the precipitation bias with increasing resolution found here are consistent over ocean with those found by Johnson et al. (2016) in MetUM-GA3. However, the latter study did not find the improvement in the bias over India when moving from 200 km grid spacing to 90 km which we see here for MetUM-GOML2.0, suggesting this may be linked to air-sea coupling or the change from GA3 to GA6.

At 90 km grid spacing there is very little difference in ISV of precipitation when all ocean basins are coupled (GL_{90}; figure 5b) and when only the Indian Ocean is coupled (IO_{90}; figure 13d). In the region where the most significant bias exists – over north-west India, Pakistan and the north Arabian Sea, where there is less than a tenth of the observed variance – IO_{90} is still a ~~major~~significant improvement over IO_{200} (figure 13e), especially over the Arabian Sea. In IO_{40} (figure 13f) there is almost no significant change in variance, except for an increase over the Arabian Sea at the entrance to the Persian Gulf. Over the land areas affected by the significant lack of variance in IO_{90}, variance slightly increases with resolution. As with the change in mean state, variance over India improves as resolution increases, but with a much greater change from 200 km to 90 km (two-fold or more over all of India) than from 90 km to 40 km (the change being negligible over most of the country).

We now consider the effect on the northward intraseasonal propagation of OLR (figure 14). Increasing resolution from 200 km through 90 km to 40 km slightly increases the pattern correlation against observations and gives increasingly realistic propagation speeds, albeit always slower than observed (table 2). At $0°$–$12.5°$N the speed is 1.34 m s^{-1} (IO$_{200}$ and IO$_{90}$) and 1.46 m s^{-1} (IO$_{40}$, while the observed speed is 1.61 m s^{-1}); and at $12.5°$–$20°$N it is 1.93 m s^{-1} (IO$_{200}$) and 2.42 m s^{-1} (IO$_{90}$ and

5   IO$_{40}$), while the observed speed is 3.22 m s^{-1}). The phase relationship between OLR and SST is correct at all three resolutions in figure 14. The southward branch of propagation is not distinct in IO$_{200}$ and IO$_{90}$, and is present in IO$_{40}$ but is substantially too slow.

The amplitudes of BSISO1 phase composites are shown for the three Indian Ocean coupling experiments in figure 15. The rates of decay of propagation events are similar to those seen earlier in figure 12, with events starting in phases 2 and 3 tending

10   to decay too slowly, and those starting in phases 4 and 5 tending to decay too quickly (except IO$_{40}$). However, none of the resolutions consistently outperforms the others, so the longevity of propagation events is not systematically improved by using any particular grid box size.

4   Discussion and conclusions

This study has evaluated the simulation of the ISM in MetUM-GOML2.0, which uses a mixed layer ocean (with vertical mixing

15   but no advection) coupled to the MetUM atmosphere, with atmosphere and ocean at the same resolution. We have investigated the effects of regional air-sea coupling (by switching off the mixed layer ocean in certain regions and imposing SST there) and horizontal resolution. Through a flux correction technique we are able to investigate each of these in a framework in which the ocean mean state is constrained to observations, so differences in SST biases are minimized between experiments, allowing us to investigate changes to model configuration without the complication of knock-on effects from a changing basic state.

20   All experiments contain biases in JJAS precipitation and 850 hPa wind. For example, there is a severe dry bias over India (with a rainfall deficit of over 70% in much of the country) and the Maritime Continent, and a wet bias over the north Indian Ocean and the tropical Pacific. Similar biases have been seen in other MetUM experiments (e.g., Johnson et al., 2016) and in the National Centers for Environmental Prediction Climate Forecast System model version 2 (NCEP CFSv2; Goswami et al., 2014; Bombardi et al., 2015).

25   Coupling in the Indian Ocean (shown by the difference between GL$_{90}$ and AO_PO$_{90}$), or Pacific and Atlantic Oceans (GL$_{90}$ and IO$_{90}$) degrades the atmospheric JJAS mean state over the sea, in particular over the west tropical Pacific and the Indian Oceans. By comparing with atmosphere-only experiments forced with the GL$_{90}$ SST but with either ISV or IAV removed, it was shown that basic state degradations are due to small SST biases introduced with coupling (section 3.1).

Further experiments (see table 3 for details) which were not presented in section 3 for brevity confirm these conclusions.

30   For example, AO_PO$_{90}$[$\overline{\text{GL}}$] has no coupling in the Indian Ocean, but has the same mean SST as GL$_{90}$ there. Therefore, the only difference between AO_PO$_{90}$[$\overline{\text{GL}}$] and AO_PO$_{90}$ is the mean Indian Ocean SST. The JJAS mean precipitation difference between AO_PO$_{90}$[$\overline{\text{GL}}$] and AO_PO$_{90}$ (not shown) is almost identical to the difference between GL$_{90}$ and AO_PO$_{90}$ (figure 3a). Thus, the effect of introducing coupling in the Indian Ocean (the latter comparison) is very similar to the effect of just intro-

ducing SST biases in the same region (the former comparison), further supporting the conclusion that the change in mean state due to coupling is attributable to the introduction of SST biases.

Similar conclusions can be drawn for the Pacific. The effect of Pacific Ocean coupling is indicated by comparing IO_{90} with IO_PO_{90}. The wet bias over the Pacific Ocean exists in IO_{90} but is considerably worse in IO_PO_{90}; the Maritime Continent dry bias, which is mostly absent in IO_{90}, is substantial in IO_PO_{90}; and the strong westerly jet which erroneously extends over the north tropical Pacific is much stronger in IO_PO_{90}. These all suggest that coupling degrades the local basic state in the Pacific just as in the Indian Ocean. Furthermore, the mean states in $ATM_{90}[\overline{GL}]$ and $AO\_PO_{90}[\overline{GL}]$, which have the same SST in the Indian Ocean and very similar SST biases in the Pacific and Atlantic, are almost the same, consistent with differences in atmospheric mean state depending on differences in SST mean state only. Similarly, in $ATM_{90}[\widetilde{IO}]$ and $ATM_{90}[\widetilde{GL}]$, in which the SSTs are similar in the Indian Ocean but differ in the Pacific and Atlantic, the only substantial mean state differences in the atmospheric mean state are outside the Indian Ocean.

The coupled SST biases responsible for the degradation of the atmospheric mean state are a limitation of this model, as they have been minimized by the ocean flux correction technique yet are non-zero (section 2.1). The reason why these biases remain is not fully understood. One possibility is due to errors in the mean wind stress. For example, in figure 2e the wind speed is too strong in GL_{90} in the southern tropical Indian Ocean, which could explain the cold bias there (figure 4) due to excessive wind-driven mixing or evaporative cooling. This cold bias is not easily removed. The 15-day relaxation time scale used in the correction technique was chosen by Hirons et al. (2015) after experimentation with a range of values; even a 1-day time scale was not enough to remove SST biases as heat added to the ocean to correct the cold bias is quickly mixed down by the strong surface winds.

Consistent with the severe dry bias over India in MetUM-GOML2.0, there is also a significant lack of ISV over the same region. The 24–70-day bandpass filtered variance is very low (e.g., for precipitation GL_{90} has less than 10% of the observed variance over west India; figure 5a); and the BSISO, while exhibiting reasonably realistic propagation in terms of progression from one BSISO1 phase to the next (section 3.3), has almost no associated precipitation anomalies over most of India (figure 10b). Thus, although the active-break cycle is simulated over most of south-east Asia, the Indian monsoon is in near-permanent break conditions in the model. However, the modelled ISV in the BoB is very close to that in GPCP precipitation and ERA-Interim $u850$. Thus, MetUM-GOML2.0 is more realistic in this sense than NCEP CFSv2 (which is coupled with a full dynamical ocean), in which there is excessive ISV in the BoB as well as in the east Arabian Sea and east equatorial Indian Ocean (Goswami et al., 2014).

The oscillation consists of northward propagation of convection over the Indian Ocean, BoB and India, as well as shorter-lived southward propagation over the Indian Ocean in the southern hemisphere. The propagation was investigated using lag correlation propagation diagrams (figure 6). The lag correlations of OLR change slightly between experiments but there is no significant overall impact of local coupling, as shown by the fact that the pattern correlations with observations vary little by experiment (table 2). The largest differences tend to be found in the southward branch of the propagation, and in the northward branch up to around 5°N. In these regions, having coupling – in particular in the Indian Ocean – is beneficial, with stronger and more coherent simulated propagation. This improvement with coupling is consistent with DeMott et al. (2011, 2014) (in

the Community Climate System Model (CCSM) and Community Atmosphere Model (CAM)) and Fu and Wang (2004) (in ECHAM4).

We note that in MetUM-GOML2.0 coupling acts to degrade the basic state but generally to improve ISV and propagation. Other studies have shown changes in ISV, especially the MJO, in conjunction with changes in mean state, but a poorer mean state is not always associated with improved ISV as here. In atmosphere-only configurations of the MetUM, increasing the rate of mixing entrainment and detrainment for deep- and mid-level convection affects the tropical mean state precipitation (Bush et al. (2015); using GA3), in particular producing more rainfall over the north-west tropical Pacific Ocean and less over the equatorial Indian Ocean and Maritime Continent. These increases in entrainment and detrainment rates also improve MJO forecast skill (Klingaman and Woolnough (2014a); using GA2). Furthermore, Inness et al. (2003) improved the strength of MJO propagation through the Maritime Continent by reducing biases in SST and wind in the coupled Hadley Centre MetUM (HadCM3), through flux adjustments.

Studies with other models have also shown relationships between changes in mean state and ISV. Kim et al. (2011) performed ten experiments with five atmosphere-only GCMs and discovered a systematic difference in boreal summer mean state precipitation between those experiments with strong ISV and weak ISV, with stronger ISV being associated with excess rainfall over the south Asian and north-west Pacific monsoon regions. Studies with ECHAM4 have shown that the simulated MJO is sensitive to the choice of prescribed SST (Liess and Bengtsson, 2004), with an experiment by Liess et al. (2004) showing an improved MJO when the AGCM is forced with SSTs from a coupled version of the model rather than observed SST. Sperber (2004) found biases in SST and wind to degrade MJO propagation, in CCSM2.

In the present study, SST IAV (when coupling is switched on; c.f. GL_{90} and $ATM_{90}[\overline{GL}]$) affects the intraseasonal propagation (figures 6b,f), although it does not impact the mean state (not shown). The interannual standard deviation of JJAS SST in GL_{90} is on the order $0.25°C$ in the tropical Indian Ocean. A question which remains unanswered is why the SST IAV should have an effect on the ISV of convection.

The effect of resolution was investigated by comparing experiments with only the Indian Ocean coupled, at three resolutions (section 3.4). The mean state precipitation improves somewhat when changing from 200 km to 90 km grid spacing, but there is little change when increasing resolution again to 40 km (figures 13a–c). A similar result was found by Ogata et al. (2017) when increasing resolution in both the MetUM GA3 and the Meteorological Research Institute of Japan atmosphere-only model (MRI-AGCM3.2), with precipitation increasing over India, the Maritime Continent and the Indian Ocean just south of the equator, and reducing over the tropical Pacific and the Indian Ocean just north of the equator. GL_{90} also shows an improved mean state over GL_{200} (not shown) but the difference over the Pacific Ocean is smaller than for IO_{200} and IO_{90}. Thus, resolution has less of an impact when there is local coupling than when the SST is prescribed. Increasing resolution also improves intraseasonal propagation and the BSISO, but only to a minor extent. Ogata et al. (2017) showed that in MRI-AGCM3.2 the intraseasonal propagation also strengthens with increasing resolution, although they found that the ISV in MetUM GA3 weakened. However, they used an atmosphere-only model with a different MetUM configuration from the present study (GA3 rather than GA6).

This study has shown that although there is an impact from including local air-sea interactions on simulating the processes responsible in the ISM using a mixed-layer ocean, these impacts are not always beneficial, with an overall worsening of the mean-state biases due to SST biases. However, there ~~is a~~are slight improvements to the simulation of the active-break cycle and BSISO.

5 *Code and data availability.* The MetUM was used under licence from the UK Met Office; for details, see https://www.metoffice.gov.uk/ research/modelling-systems/unified-model. The KPP model is freely available from a Subversion repository at https://puma.nerc.ac.uk/ svn/KPP_ocean_svn/KPP_ocean; for details, see https://puma.nerc.ac.uk/trac/KPP_ocean. Data used to create the figures in this paper and associated code may be found at https://doi.org/10.6084/m9.figshare.c.4186493.v1. Other model output is stored on JASMIN (http: //www.jasmin.ac.uk) and will be made available on request.

10 *Competing interests.* The authors have no competing interests to declare.

Acknowledgements. SCP was supported by a grant from the UK Natural Environment Research Council (NERC; NE/L013800/1). NPK was supported by a NERC Independent Research Fellowship (NE/L010976/1). Assembly of MetUM-GOML2.0 and development of MC-KPP was supported by the National Centre for Atmospheric Science, a NERC collaborative centre, under contract R8/H12/83/001. AVHRR OLR data were provided by the NOAA/OAR/ESRL PSD, Boulder, Colorado, USA, from their Web site at http://www.esrl.noaa.gov/psd.
15 The authors are grateful to Prof. Adrian Matthews, Prof. P. N. Vinayachandran and other colleagues on the BoBBLE project for productive discussions on this research; ~~and~~ to Dr Ben Harvey for helpful conversations on filtering of time series; and to two anonymous reviewers for their suggestions for improvements to the manuscript.

References

Bombardi, R. J., Schneider, E. K., Marx, L., Halder, S., Singh, B., Tawfik, A. B., Dirmeyer, P. A., and Kinter, J. L.: Improvements in the Representation of the Indian Summer Monsoon in the NCEP Climate Forecast System Version 2, Clim. Dyn., 45, 2485–2498, https://doi.org/10.1007/s00382-015-2484-6, 2015.

5 Bush, S. J., Turner, A. G., Woolnough, S. J., Martin, G. M., and Klingaman, N. P.: The effect of increased convective entrainment on Asian monsoon biases in the MetUM general circulation model, Q. J. R. Meteorol. Soc., 141, 311–326, https://doi.org/10.1002/qj.2371, 2015.

Dee, D. P., Uppala, S. M., Simmons, A. J., Berrisford, P., Poli, P., Kobayashi, S., Andrae, U., Balmaseda, M. A., Balsamo, G., Bauer, P., Bechtold, P., Beljaars, A. C. M., van de Berg, L., Bidlot, J., Bormann, N., Delsol, C., Dragani, R., Fuentes, M., Geer, A. J., Haimberger, L., Healy, S. B., Hersbach, H., Hólm, E. V., Isaksen, L., Kållberg, P., Köhler, M., Matricardi, M., McNally, A. P., Monge-Sanz, B. M., Mor-
10 crette, J.-J., Park, B.-K., Peubey, C., de Rosnay, P., Tavolato, C., Thépaut, J.-N., and Vitart, F.: The ERA-Interim reanalysis: configuration and performance of the data assimilation system, Q. J. R. Meteorol. Soc., 137, 553–597, https://doi.org/10.1002/qj.828, 2011.

DeMott, C. A., Stan, C., Randall, D. A., Kinter, J. L., and Khairoutdinov, M.: The Asian monsoon in the superparameterized CCSM and its relationship to tropical wave activity, J. Clim., 24, 5134–5156, https://doi.org/10.1175/2011JCLI4202.1, 2011.

DeMott, C. A., Stan, C., Randall, D. A., and Branson, M. D.: Intraseasonal variability in coupled GCMs: The roles of ocean feedbacks and
15 model physics, J. Clim., 27, 4970–4995, https://doi.org/10.1175/JCLI-D-13-00760.1, 2014.

DeMott, C. A., Klingaman, N. P., and Woolnough, S. J.: Atmosphere-Ocean Coupled Processes in the Madden-Julian Oscillation, Rev. Geophys., 53, 1099–1154, https://doi.org/10.1002/2014RG000478, 2015.

Duchon, C. E.: Lanczos Filtering in One and Two Dimensions, J. Appl. Meteorol., 18, 1016–1022, https://doi.org/10.1175/1520-0450(1979)018<1016:LFIOAT>2.0.CO;2, 1979.

20 Fang, Y., Wu, P., Mizielinski, M. S., Roberts, M. J., Wu, T., Li, B., and Vidale, P. L.: High-resolution simulation of the boreal summer intra-seasonal oscillation in Met Office Unified Model, J. Clim., 143, 362–373, https://doi.org/10.1002/qj.2927, 2017.

Fu, X. and Wang, B.: Differences of boreal summer intraseasonal oscillations simulated in an atmosphere-ocean coupled model and an atmosphere-only model, J. Clim., 17, 1263–1271, https://doi.org/10.1175/1520-0442(2004)017<1263:DOBSIO>2.0.CO;2, 2004.

Gadgil, S. and Gadgil, S.: The Indian Monsoon, GDP and Agriculture, Econ. Polit. Wkly., 41, 4887–4895, 2006.

25 Goswami, B. B. N., Deshpande, M., Mukhopadhyay, P., Saha, S. K., Rao, S. A., Murthugudde, R., and Goswami, B. B. N.: Simulation of monsoon intraseasonal variability in NCEP CFSv2 and its role on systematic bias, Clim. Dyn., 43, 2725–2745, https://doi.org/10.1007/s00382-014-2089-5, 2014.

Halley, E.: An Historical Account of the Trade Winds, and Monsoons, Observable in the Seas between and Near the Tropicks, with an Attempt to Assign the Phisical Cause of the Said Winds, Philos. Trans. R. Soc. London, 16, 153–168, 1686.

30 Hendon, H. H. and Glick, J.: Intraseasonal air-sea interaction in the tropical Indian and Pacific Oceans, J. Clim., 10, 647–661, https://doi.org/10.1175/1520-0442(1997)010<0647:IASIIT>2.0.CO;2, 1997.

Hirons, L. C., Klingaman, N. P., and Woolnough, S. J.: MetUM-GOML1: A Near-Globally Coupled Atmosphere–Ocean-Mixed-Layer Model, Geosci. Model Dev., 8, 363–379, https://doi.org/10.5194/gmd-8-363-2015, 2015.

Huffman, G. J., Adler, R. F., Morrissey, M. M., Bolvin, D. T., Curtis, S., Joyce, R., McGavock, B., and Susskind, J.: Global Precip-
35 itation at One-Degree Daily Resolution from Multisatellite Observations, J. Hydrometeorol., 2, 36–50, https://doi.org/10.1175/1525-7541(2001)002<0036:GPAODD>2.0.CO;2, 2001.

Inness, P. M., Slingo, J. M., Guilyardi, E., and Cole, J.: Simulation of the Madden-Julian Oscillation in a Coupled General Circulation Model. Part II: The Role of the Basic State, J. Clim., 16, 365–382, https://doi.org/10.1175/1520-0442(2003)016<0365:SOTMJO>2.0.CO;2, 2003.

Johnson, S. J., Levine, R. C., Turner, A. G., Martin, G. M., Woolnough, S. J., Schiemann, R., Mizielinski, M. S., Roberts, M. J., Vidale, P. L., Demory, M.-E., and Strachan, J.: The Resolution Sensitivity of the South Asian Monsoon and Indo-Pacific in a Global 0.35° AGCM, Clim. Dyn., 46, 807–831, https://doi.org/10.1007/s00382-015-2614-1, 2016.

Kim, D., Sobel, A. H., Maloney, E. D., Frierson, D. M. W., and Kang, I.-S.: A Systematic Relationship between Intraseasonal Variability and Mean State Bias in AGCM Simulations, J. Appl. Meteorol., 24, 5506–5520, https://doi.org/10.1175/2011JCLI4177.1, 2011.

Klingaman, N. P. and Woolnough, S. J.: Using a case-study approach to improve the Madden-Julian oscillation in the Hadley Centre model, Q. J. R. Meteorol. Soc., 140, 2491–2505, https://doi.org/10.1002/qj.2314, 2014a.

Klingaman, N. P. and Woolnough, S. J.: The role of air-sea coupling in the simulation of the Madden-Julian oscillation in the Hadley Centre model, Q. J. R. Meteorol. Soc., 140, 2272–2286, https://doi.org/10.1002/qj.2295, 2014b.

Klingaman, N. P., Inness, P. M., Weller, H., and Slingo, J. M.: The Importance of High-Frequency Sea Surface Temperature Variability to the Intraseasonal Oscillation of Indian Monsoon Rainfall, J. Clim., 21, 6119–6140, https://doi.org/10.1175/2008JCLI2329.1, 2008.

Klingaman, N. P., Woolnough, S. J., Weller, H., and Slingo, J. M.: The Impact of Finer-Resolution Air-Sea Coupling on the Intraseasonal Oscillation of the Indian Monsoon, J. Clim., 24, 2451–2468, https://doi.org/10.1175/2010JCLI3868.1, 2011.

Large, W. G., McWilliams, J. C., and Doney, S. C.: Oceanic Vertical Mixing: A Review and a Model with a Nonlocal Boundary Layer Parameterization, Rev. Geophys., 32, 363–403, 1994.

Lau, K.-M. and Chan, P. H.: Aspects of the 40-50 Day Oscillation during the Northern Summer as Inferred from Outgoing Longwave Radiation, Mon. Weather Rev., 114, 1354–1367, https://doi.org/10.1175/1520-0493(1986)114<1354:AOTDOD>2.0.CO;2, 1986.

Lee, J.-Y., Wang, B., Wheeler, M. C., Fu, X., Waliser, D. E., and Kang, I.-S.: Real-Time Multivariate Indices for the Boreal Summer Intraseasonal Oscillation over the Asian Summer Monsoon Region, Clim. Dyn., 40, 493–509, https://doi.org/10.1007/s00382-012-1544-4, 2013.

Liess, S. and Bengtsson, L.: The intraseasonal oscillation in ECHAM4 Part II: sensitivity studies, Clim. Dyn., 22, 671–688, https://doi.org/10.1007/s00382-004-0407-z, 2004.

Liess, S., Bengtsson, L., and Arpe, K.: The intraseasonal oscillation in ECHAM4 Part I: coupled to a comprehensive ocean model, Clim. Dyn., 22, 653–669, https://doi.org/10.1007/s00382-004-0406-0, 2004.

Lin, J.-L., Weickmann, K. M., Kiladis, G. N., Mapes, B. E., Schubert, S. D., Suarez, M. J., Bacmeister, J. T., and Lee, M.-I.: Subseasonal variability associated with Asian summer monsoon simulated by 14 IPCC AR4 coupled GCMs, J. Clim., 21, 4541–4567, https://doi.org/10.1175/2008JCLI1816.1, 2008.

Ogata, T., Johnson, S. J., Schiemann, R., Demory, M.-E., Mizuta, R., Yoshida, K., and Arakawa, O.: The resolution sensitivity of the Asian summer monsoon and its inter-model comparison between MRI-AGCM and MetUM, Clim. Dyn., 49, 3345–3361, https://doi.org/10.1007/s00382-016-3517-5, 2017.

Peatman, S. C., Matthews, A. J., and Stevens, D. P.: Propagation of the Madden–Julian Oscillation and scale interaction with the diurnal cycle in a high-resolution GCM, Clim. Dyn., 45, 2901–2918, https://doi.org/10.1007/s00382-015-2513-5, 2015.

Riley, K. F., Hobson, M. P., and Bence, S. J.: Mathematical Methods for Physics and Engineering, Cambridge University Press, 3rd edn., 2007.

Ringer, M. A., Martin, G. M., Greeves, C. Z., Hinton, T. J., James, P. M., Pope, V. D., Scaife, A. A., Stratton, R. A., Inness, P. M., Slingo, J. M., and Yang, G.-Y.: The Physical Properties of the Atmosphere in the New Hadley Centre Global Environmental Model (HadGEM1). Part II: Aspects of Variability and Regional Climate, J. Clim., 19, 1302–1326, 2006.

Smith, D. M. and Murphy, J. M.: An Objective Ocean Temperature and Salinity Analysis using Covariances from a Global Climate Model, J. Geophys. Res., 112, C02 022, https://doi.org/10.1029/2005JC003172, 2007.

Sperber, K. R.: Madden-Julian variability in NCAR CAM2.0 and CCSM2.0, Clim. Dyn., 23, 259–278, https://doi.org/10.1007/s00382-004-0447-4, 2004.

Sperber, K. R., Annamalai, H., Kang, I.-S., Kitoh, A., Moise, A., Turner, A. G., Wang, B., and Zhou, T.: The Asian Summer Monsoon: an Intercomparison of CMIP5 vs. CMIP3 Simulations of the Late 20th Century, Clim. Dyn., 41, 2711–2744, https://doi.org/10.1007/s00382-012-1607-6, 2013.

Taylor, K. E., Williamson, D. L., and Zwiers, F.: The Sea Surface Temperature and Sea-Ice Concentration Boundary Conditions for AMIP II Simulations, Tech. Rep. 60, 2000.

Taylor, K. E., Stouffer, R. J., and Meehl, G. A.: An Overview of CMIP5 and the Experiment Design, Bull. Am. Meteorol. Soc., 93, 485–498, https://doi.org/10.1175/BAMS-D-11-00094.1, 2012.

Trenberth, K. E.: Some Effects of Finite Sample Size and Persistence on Meteorological Statistics. Part I: Autocorrelations, Mon. Weather Rev., 112, 2359–2368, https://doi.org/10.1175/1520-0493(1984)112<2359:SEOFSS>2.0.CO;2, 1984.

Turner, A. G. and Annamalai, H.: Climate change and the South Asian summer monsoon, Nat. Clim. Chang., 2, 587–595, https://doi.org/10.1038/NCLIMATE1495, 2012.

Waliser, D. E., Jin, K., Kang, I.-S., Stern, W. F., Schubert, S. D., Wu, M. L. C., Lau, W. K.-M., Lee, M.-I., Krishnamurthy, V., Kitoh, A., Meehl, G. A., Galin, V. Y., Satyan, V., Mandke, S. K., Wu, G., Liu, Y., and Park, C.-K.: AGCM simulations of intraseasonal variability associated with the Asian summer monsoon, Clim. Dyn., 21, 423–446, https://doi.org/10.1007/s00382-003-0337-1, 2003.

Walters, D. N., Boutle, I. A., Brooks, M., Melvin, T., Stratton, R. A., Vosper, S., Wells, H., Williams, K. D., Wood, N., Allen, T., Bushell, A. C., Copsey, D., Earnshaw, P. D., Edwards, J. M., Gross, M., Hardiman, S., Harris, C. M., Heming, J., Klingaman, N. P., Levine, R. C., Manners, J. C., Martin, G. M., Milton, S. F., Mittermaier, M., Morcrette, C. J., Riddick, T., Roberts, M. J., Sanchez, C., Selwood, P., Stirling, A., Smith, C., Suri, D., Tennant, W., Vidale, P. L., Wilkinson, J. M., Willett, M. R., Woolnough, S. J., and Xavier, P. K.: The Met Office Unified Model Global Atmosphere 6.0/6.1 and JULES Global Land 6.0/6.1 configurations, Geosci. Model Dev., 10, 1487–1520, https://doi.org/10.5194/gmd-7-361-2014, 2017.

Wheeler, M. C. and Hendon, H. H.: An All-Season Real-Time Multivariate MJO Index: Development of an Index for Monitoring and Prediction, Mon. Weather Rev., 132, 1917–1932, 2004.

Williams, K. D., Harris, C. M., Bodas-Salcedo, A., Camp, J., Comer, R. E., Copsey, D., Fereday, D., Graham, T., Hill, R., Hinton, T. J., Hyder, P., Ineson, S., Masato, G., Milton, S. F., Roberts, M. J., Rowell, D. P., Sanchez, C., Shelly, A., Sinha, B., Walters, D. N., West, A., Woollings, T., and Xavier, P. K.: The Met Office Global Coupled Model 2.0 (GC2) Configuration, Geosci. Model Dev., 8, 1509–1524, https://doi.org/10.5194/gmd-8-1509-2015, 2015.

Yang, B., Fu, X., and Wang, B.: Atmosphere-ocean conditions jointly guide convection of the Boreal Summer Intraseasonal Oscillation: Satellite observations, J. Geophys. Res. Atmos., 113, 1–16, https://doi.org/10.1029/2007JD009276, 2008.

Yasunari, T.: Cloudiness Fluctuations Associated with the Northern Hemisphere Summer, J. Meteorol. Soc. Japan, 57, 227–242, https://doi.org/10.2151/jmsj1965.57.3_227, 1979.

Experiment	UM grid	Coupling			SST (where uncoupled)
		AO	IO	PO	
GL_{90} ("near-global")	N216	✓	✓	✓	SM07 seasonal cycle
AO_PO_{90}	N216	✓		✓	SM07 seasonal cycle
$ATM_{90}[\tilde{GL}]$	N216				31-day smoothed from GL_{90}
$ATM_{90}[\tilde{IO}]$	N216				31-day smoothed from IO_{90}
$ATM_{90}[\overline{GL}]$	N216				Seasonal cycle from GL_{90}
IO_{200}, IO_{90}, IO_{40}	N96, N216, N512		✓		SM07 seasonal cycle

Table 1. List of experiments performed. Subscripts indicate the approximate grid spacing in km at the equator. Ticks indicate the ocean basins (Atlantic Ocean, Indian Ocean and Pacific Ocean) in which the MetUM was coupled to MC-KPP. (Maps of the coupling regions are shown in figure 1.) The final column indicates the SST prescribed in regions where the atmosphere is not coupled to the mixed layer ocean.

Experiment	Propagation speed / m s^{-1}		Pattern correlation
	$0°$–$12.5°$N	$12.5°$–$20°$N	
Observations	**1.61**	**3.22**	*1.000*
GL$_{90}$	1.61	1.61	0.838
AO_PO$_{90}$	1.15	1.61	0.869
IO$_{90}$	1.34	2.42	0.893
ATM$_{90}[\tilde{GL}]$	1.15	2.42	0.867
ATM$_{90}[\tilde{IO}]$	1.34	1.93	0.884
ATM$_{90}[\overline{GL}]$	1.34	1.61	0.875
IO$_{200}$	1.34	1.93	0.847
IO$_{40}$	1.46	2.42	0.909

Table 2. Propagation speeds indicated by the green lines in figures 6 and 14; and pattern correlation between OLR lag correlations in the same figures and for observations (figure 6a).

| Experiment | UM grid | Coupling | | | SST (where uncoupled) |
		AO	IO	PO	
AO_PO$_{90}$[$\overline{\text{GL}}$]	N216	✓		✓	Seasonal cycle from GL$_{90}$
IO_PO$_{90}$	N216		✓	✓	SM07 seasonal cycle
GL$_{200}$	N96	✓	✓	✓	SM07 seasonal cycle

Table 3. List of further experiments referred to in section 4. See table 1 for full explanation.
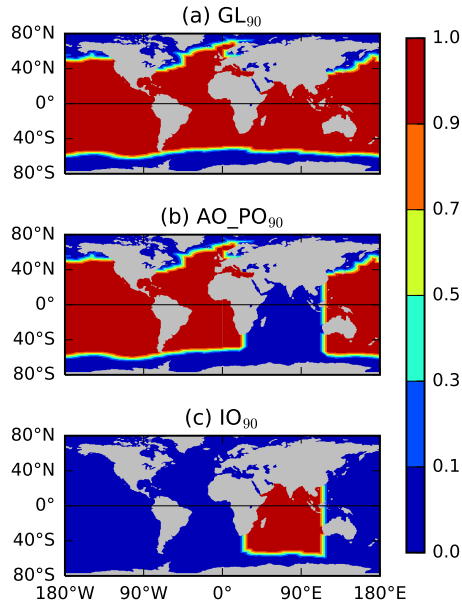
Figure 1. Coupling weights for each coupling region used in the experiments: (a) GL$_{90}$; (b) AO_PO$_{90}$; (c) IO$_{90}$. The MC-KPP SST is multiplied by the weight shown and the prescribed SST by $(1-\text{weight})$, and the sum of the two is the boundary condition to the atmospheric grid box. A $10°$ width (12 grid points) blending is applied at any boundary that is not a coastline. The weights for 200 km and 40 km experiments are the same but with 5- and 30-point blending respectively.
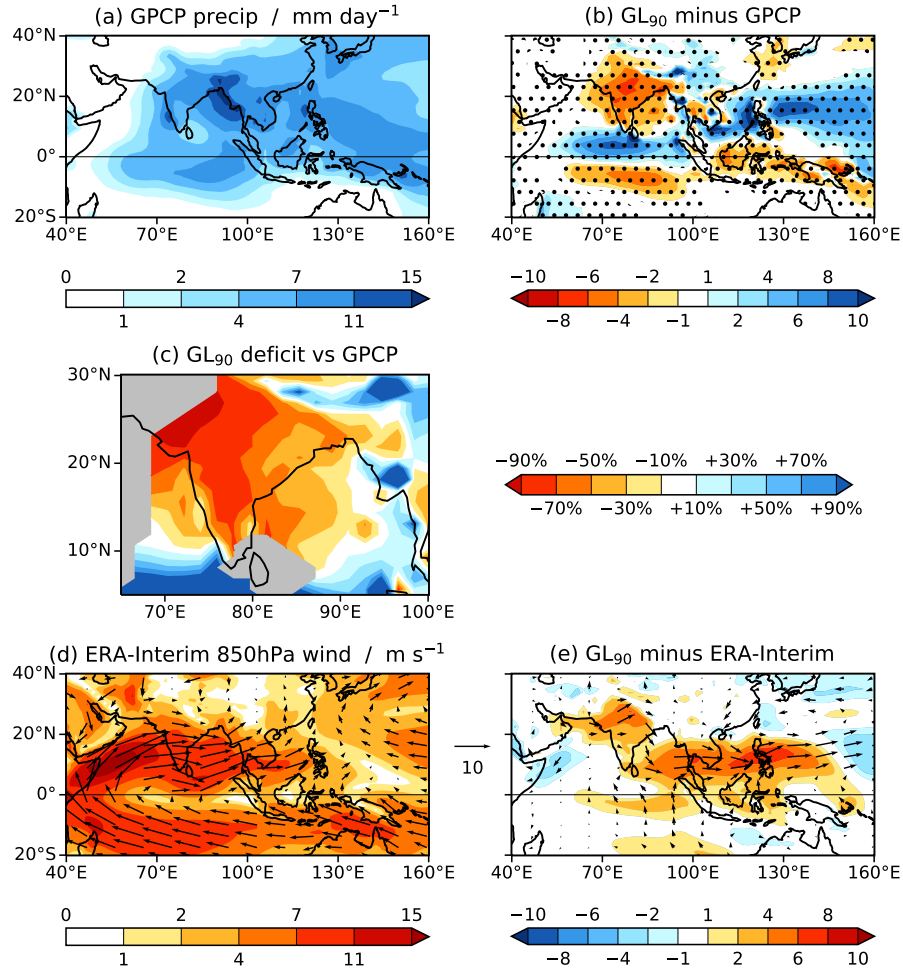
Figure 2. (a) JJAS mean precipitation from GPCP. (b) Bias in JJAS mean precipitation in GL90. Stippling indicates 99% statistical significance according to a two-tailed t-test. (c) Percentage excess (blue) and deficit (red) JJAS mean precipitation in GL90 relative to GPCP. Regions in which the GPCP climatology is below 3 mm day^{-1} are greyed out. (d) JJAS mean 850 hPa wind (vectors) and wind speed (shading) from ERA-Interim. (e) Bias in JJAS mean 850 hPa wind (vectors; shown only if statistically significant at the 99% level according to a two-tailed t-test) and wind speed (shading; bias of the wind speed, *not* magnitude of the bias vectors) in GL90.
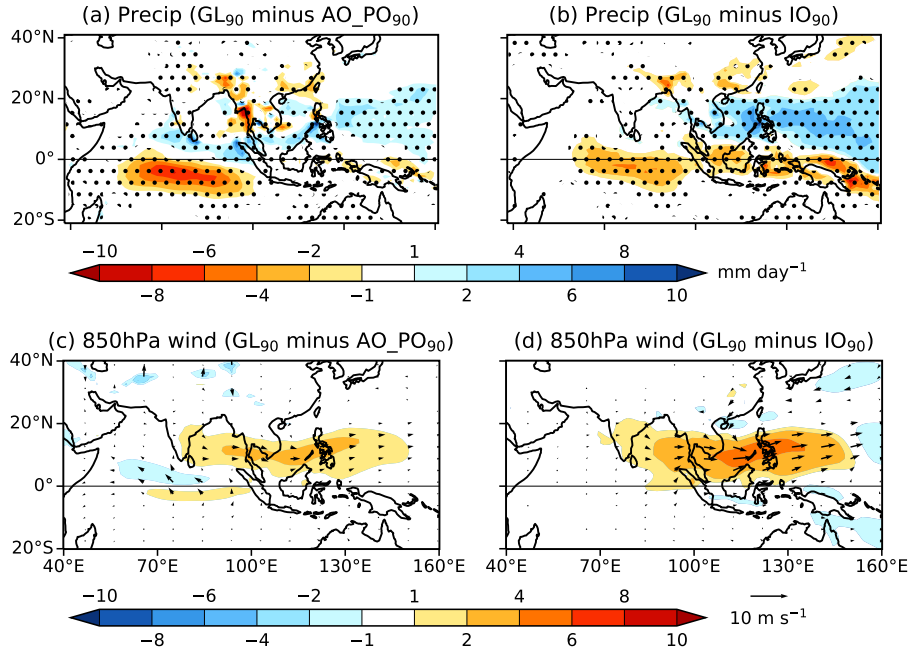
Figure 3. (a,b) JJAS mean precipitation (mm day^{-1}) in GL$_{90}$ minus that from (a) AO_PO$_{90}$, (b) IO$_{90}$. Stippling indicates 99% statistical significance according to a two-tailed t-test. (c,d) Similarly but for 850 hPa wind (m s^{-1}), with vectors (shown only if statistically significant at the 99% level according to a two-tailed t-test) and coloured shading as defined in figure 2e.
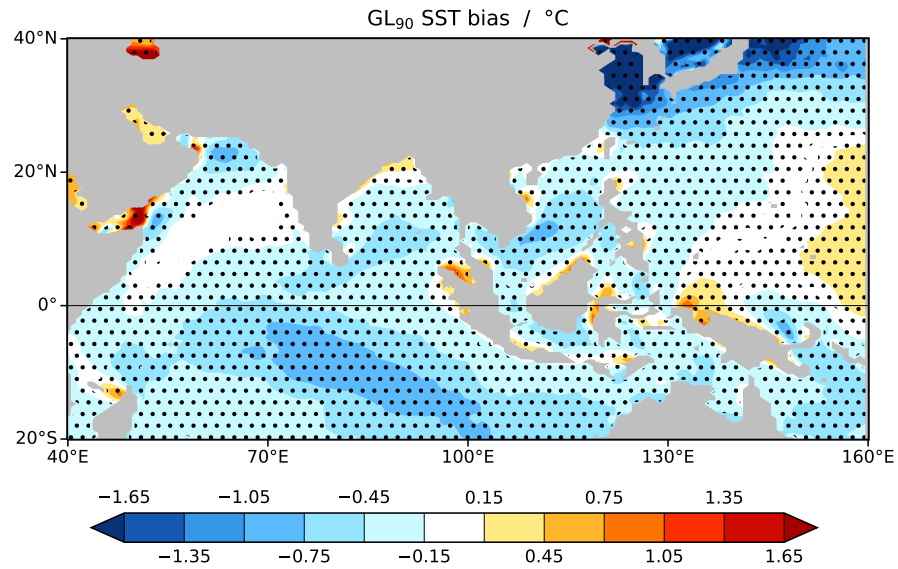
Figure 4. JJAS SST bias for GL$_{90}$ relative to SM07. Stippling indicates 99% statistical significance according to a two-tailed t-test. Land and coastally tiled points (i.e., non-zero land fraction) are in grey.
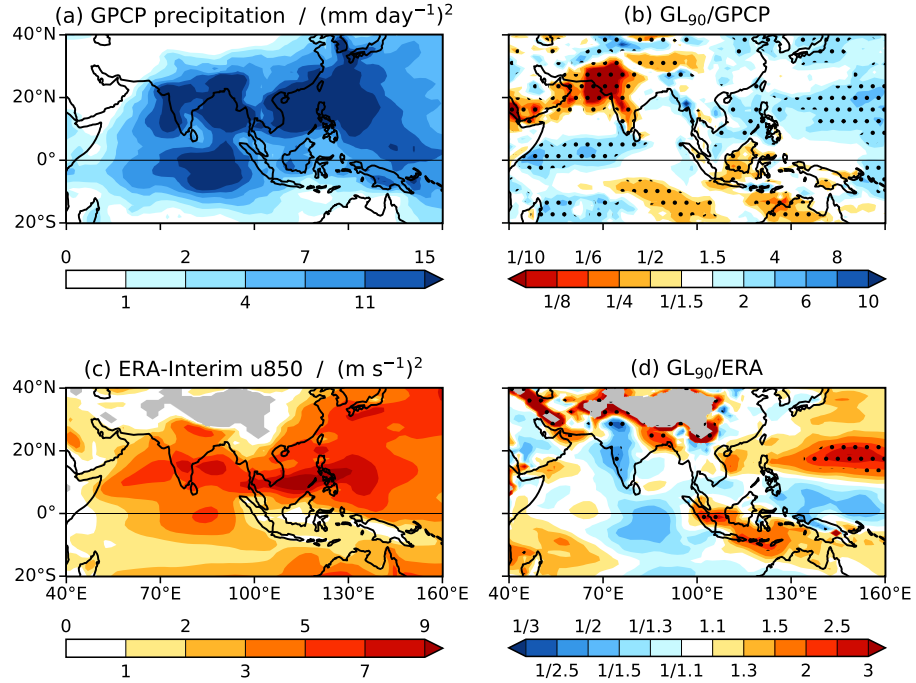
Figure 5. (a) Variance of 24–70-day bandpass filtered GPCP precipitation, for May to October only. (b) Ratio of filtered variance of precipitation from GL_{90} to that from GPCP. (c,d) As for (a,b) but for ERA-Interim $u850$, with grey shading used to mask out regions where the 850 hPa surface intersects the ground in GL_{90}; stippling indicates 95% statistical significance according to a two-tailed f-test.
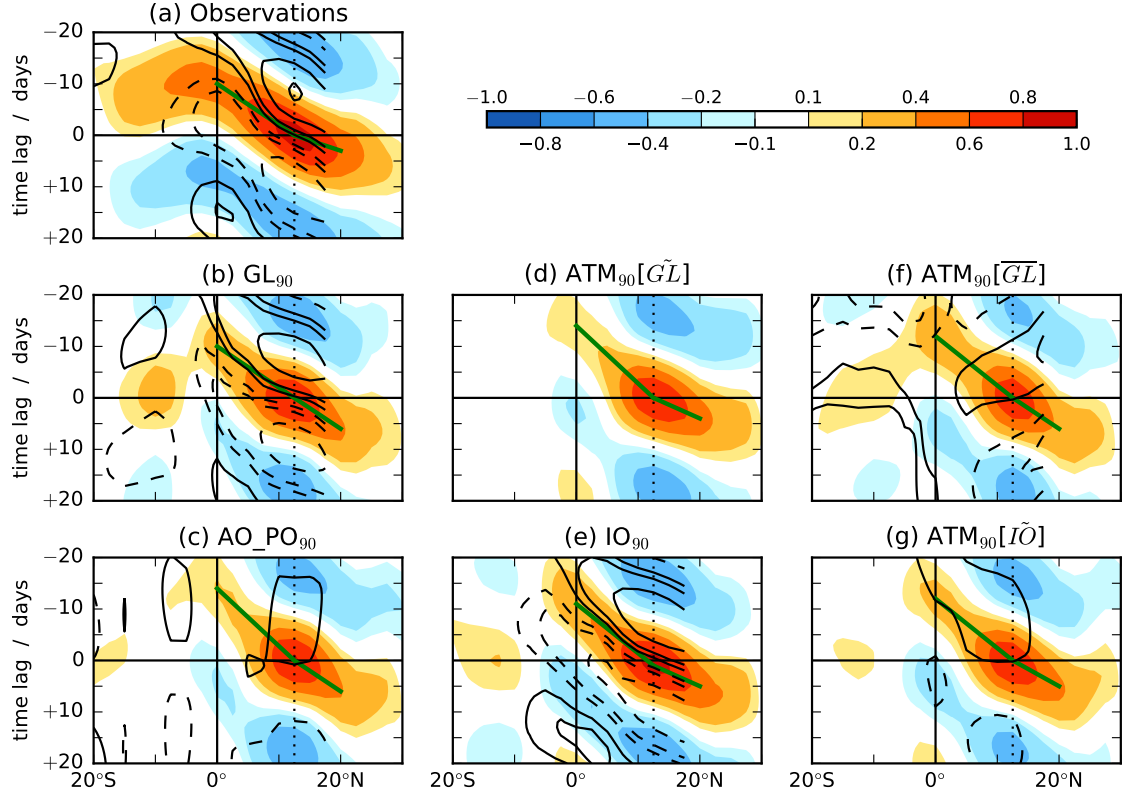
Figure 6. Intraseasonal propagation in the region $70°$–$100°$E, $20°$S–$30°$N using 24–70-day bandpass filtered data, for May to October only, illustrated by lag correlations at each latitude between zonally-averaged data and the OLR time series (also filtered) at a base point $85°$E, $12.5°$N. Coloured shading is for zonally-averaged OLR. Green lines show propagation from $0°$ to $12.5°$N, and $12.5°$ to $20°$N. Black contours are for zonally-averaged SST, with solid (dashed) contours indicating negative (positive) correlation (remembering that negative OLR anomalies correspond to increased convection) and the contour interval being the same as for the coloured shading. SST is shown up to $17.5°$N only, where half of the longitude domain is occupied by land. The vertical dotted line shows the latitude of the base point. (a) Observations/reanalysis (AVHRR OLR and ERA-Interim SST), (b) GL_{90}, (c) AO_PO_{90}, (d) $ATM_{90}[\tilde{GL}]$ (n.b., SST correlations are too small to appear), (e) IO_{90}, (f) $ATM_{90}[\overline{GL}]$, (g) $ATM_{90}[\tilde{IO}]$.
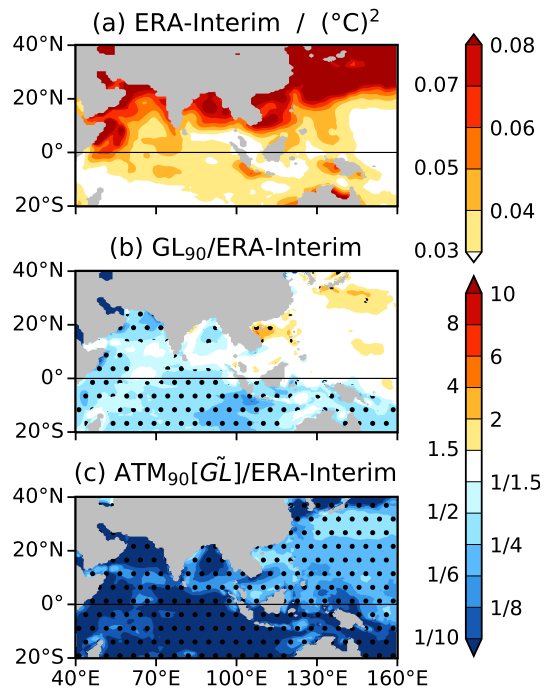
Figure 7. (a) Variance of 24–70-day bandpass filtered ERA-Interim SST, for May to October only. Ratio to ERA-Interim of (b) GL$_{90}$, (c) ATM$_{90}[\tilde{GL}]$; stippling indicates 95% statistical significance according to a two-tailed f-test.
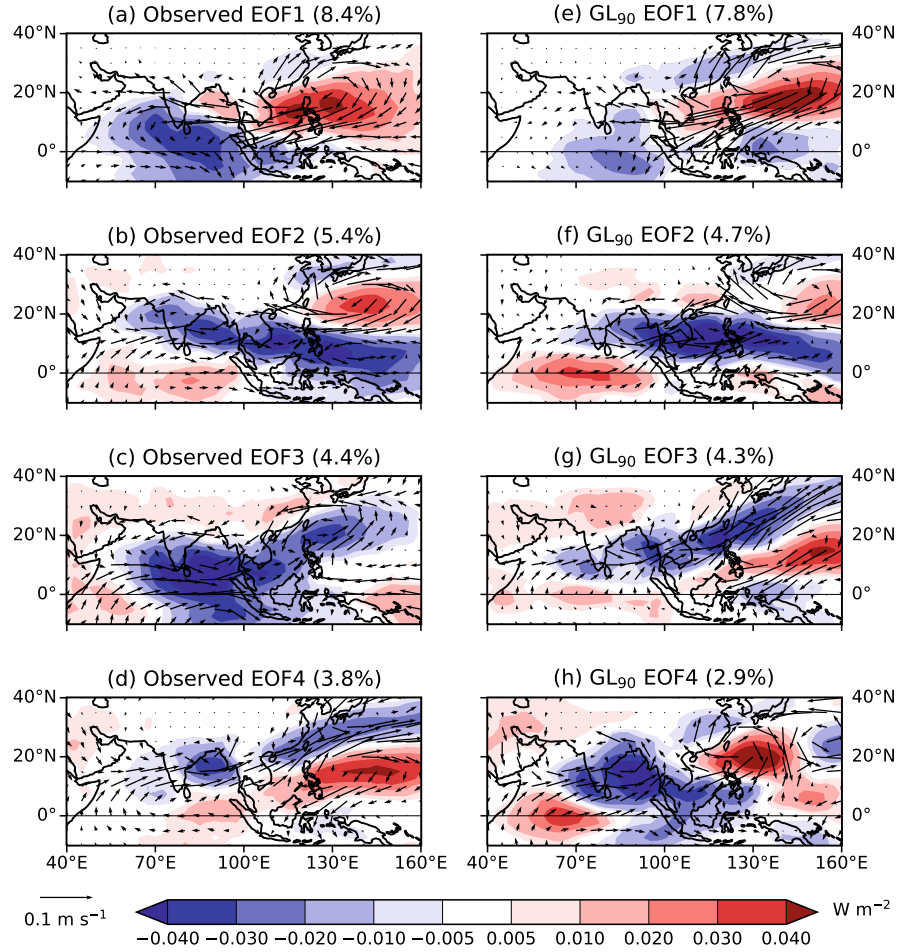
Figure 8. (a-d) MV-EOFs of OLR and $u850$, calculated from AVHRR OLR and ERA-Interim $u850$ using the method of Lee et al. (2013) (cf. their figures 2a,b and 3a,b). The meridional component of the wind plotted here was computed by regression onto the respective principal components. Figures in parentheses indicate the percentage of variance explained. (e-f) MV-EOFs calculated by the same method from GL$_{90}$.
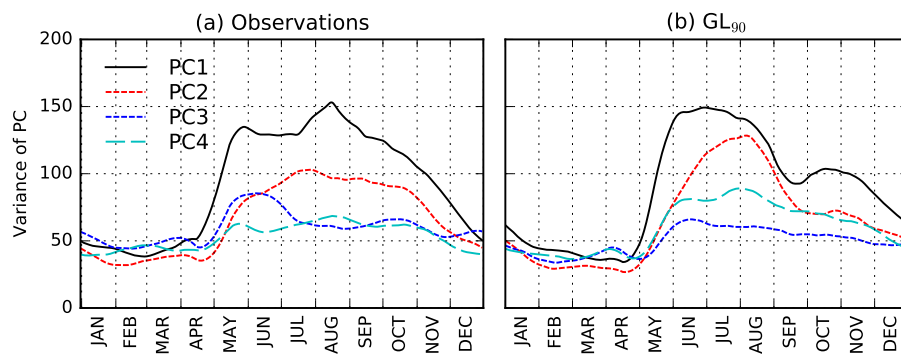
Figure 9. 30-day smoothed annual cycle of the variance of the leading four pseudo principal components for (a) AVHRR OLR and ERA-Interim $u850$, (b) GL$_{90}$. Note that year-round data have been used for the projections, even though the EOFs were computed from boreal summer data only. cf. Lee et al. (2013) figure 4.
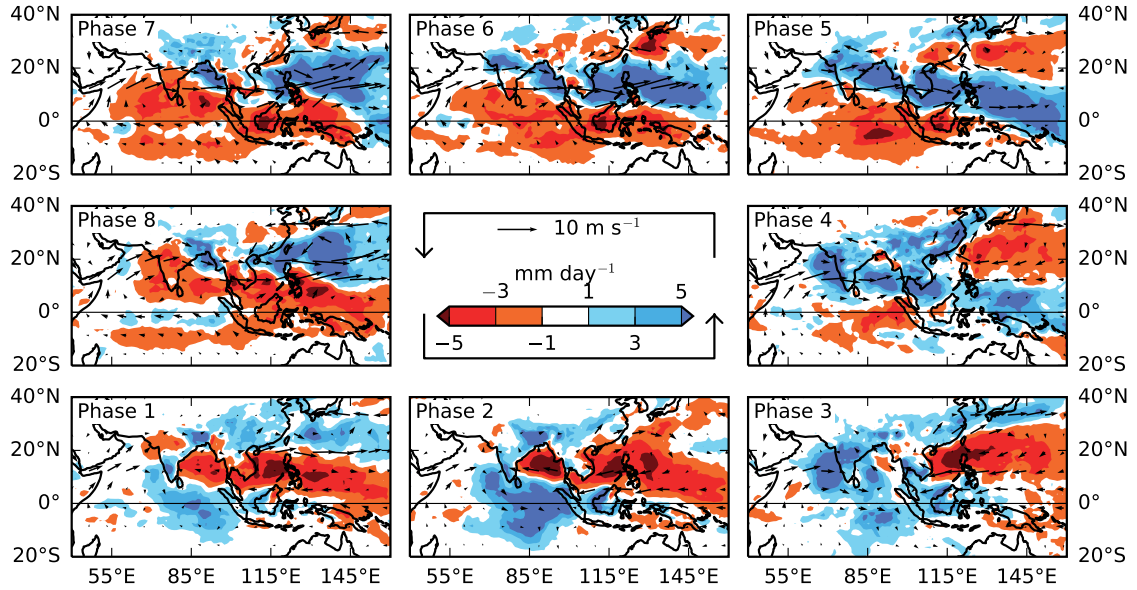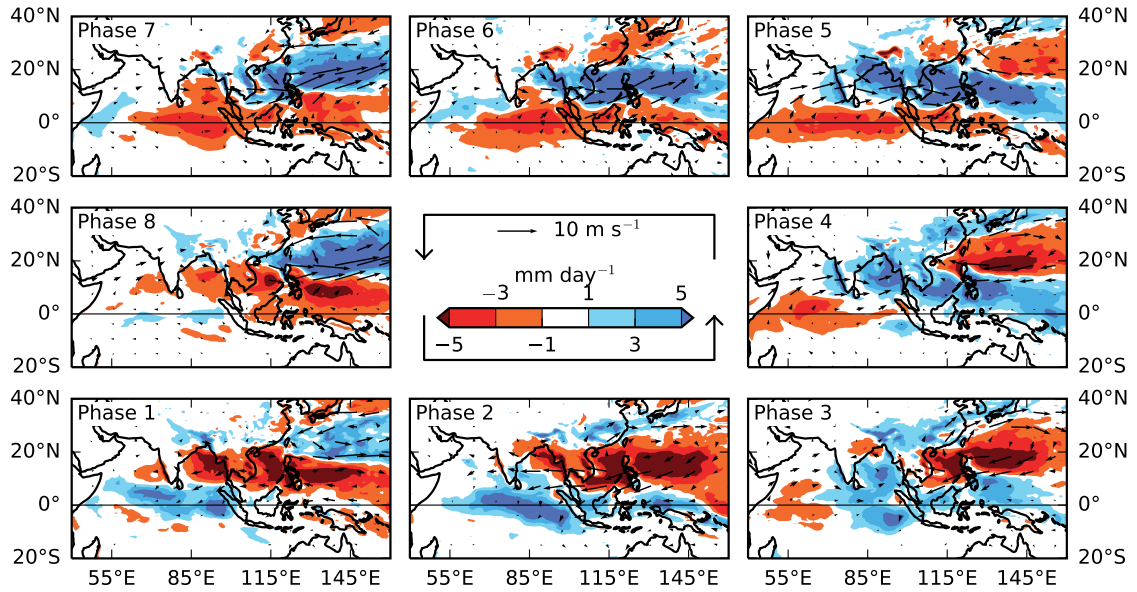
Figure 10. MJJASO anomalies in each BSISO1 phase of precipitation (shading) and 850 hPa wind (vectors; anomalies with amplitude greater than 0.5 m s⁻¹ only), for (a) observations, (b) GL₉₀. Phase 1 is in the bottom-left corner and phases continue anti-clockwise round the diagram.
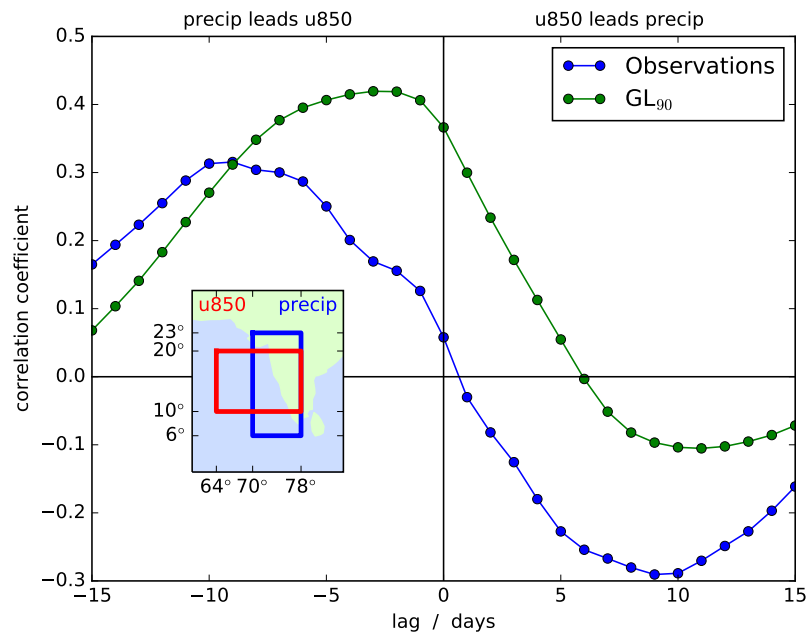
Figure 11. Lag correlation of precipitation and $u850$, averaged over the boxes shown (inset) for boreal summer (June to September), from observations (GPCP precipitation and ERA-Interim wind, 1997–2010) and GL$_{90}$.
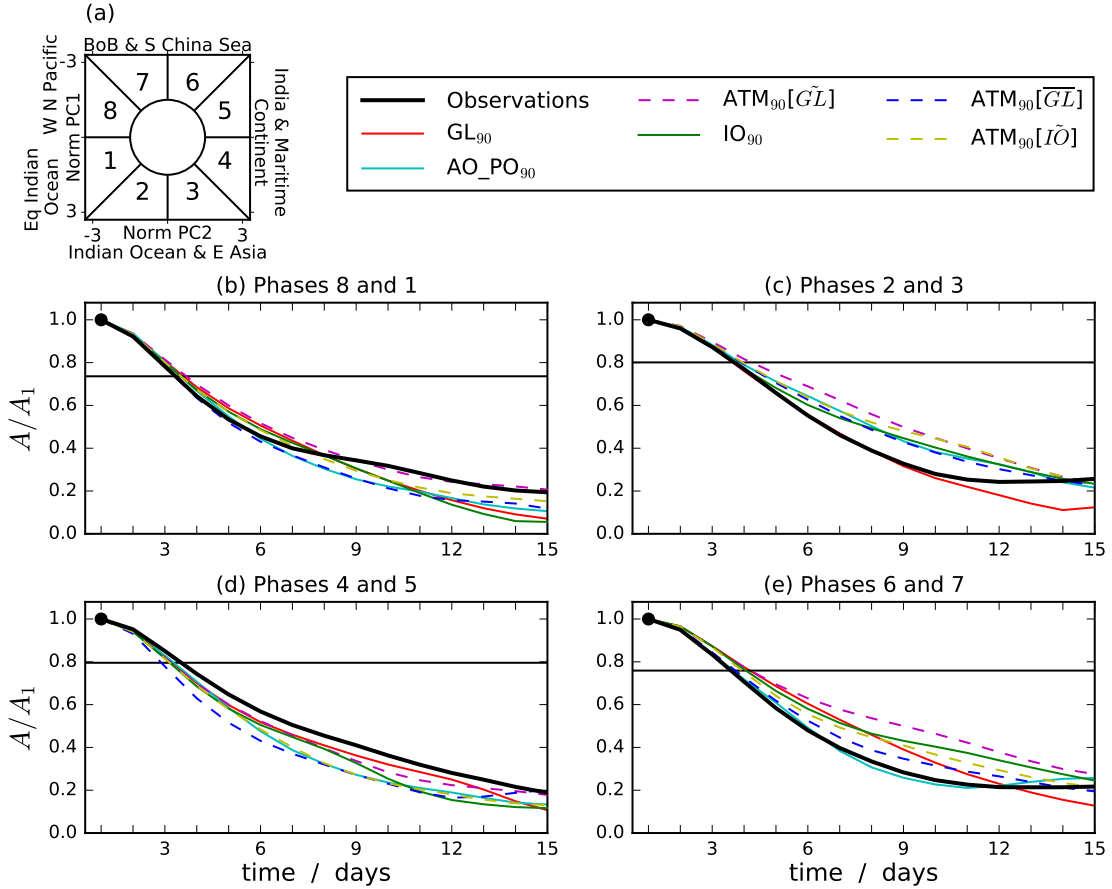
Figure 12. (a) BSISO1 phase diagram showing the eight numbered phases defined by Lee et al. (2013) and with labels indicating the regions of active convection in each. (b-e) Amplitudes A of 15-day composites of BSISO1 events starting in either of the stated phases, divided by the amplitude on the first day A_1. An event is defined as beginning on a day when the amplitude $\sqrt{\text{PC1}^2 + \text{PC2}^2} \geq 1.5$ (i.e., not inside the centre circle in panel (a)). The horizontal lines indicate $A = 1.5$ for observations.
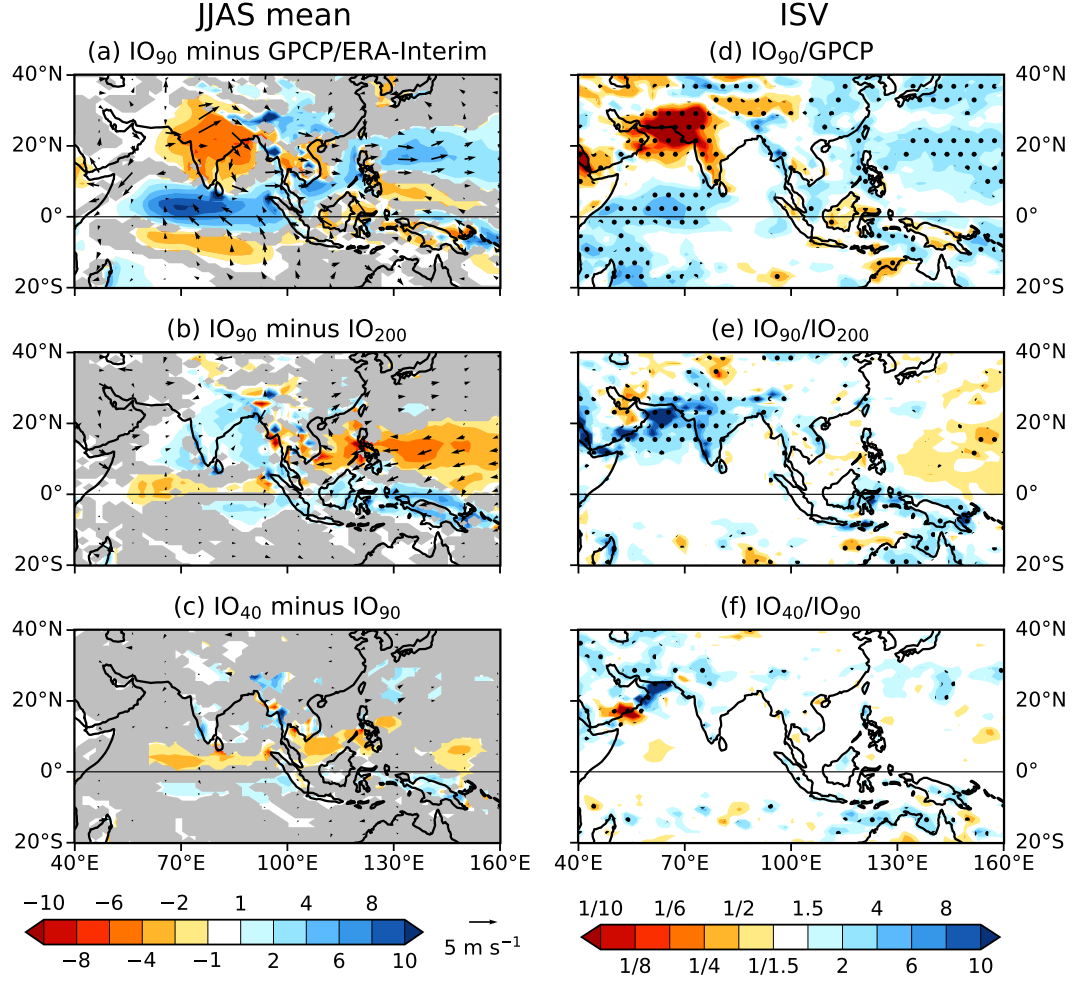
Figure 13. (a–c) JJAS mean precipitation (shading; mm day^{-1}) and 850 hPa wind (vectors; m s^{-1}; values below 1 m s^{-1} not shown): (a) IO$_{90}$ minus GPCP/ERA-Interim, (b) IO$_{90}$ minus IO$_{200}$, (c) IO$_{40}$ minus IO$_{90}$; grey shading indicates precipitation is statistically *insignificant* at the 99% level according to a two-tailed t-test; vectors (black) are shown only if statistically significant at the 99% level according to a two-tailed t-test. (d-f) Ratio of MJJASO variance of 24–70-day bandpass filtered precipitation, in (mm day^{-1})^2: (d) IO$_{90}$ over GPCP observations, (e) IO$_{90}$ over IO$_{200}$, (f) IO$_{40}$ over IO$_{90}$; stippling indicates 99% statistical significance according to a two-tailed t-test.
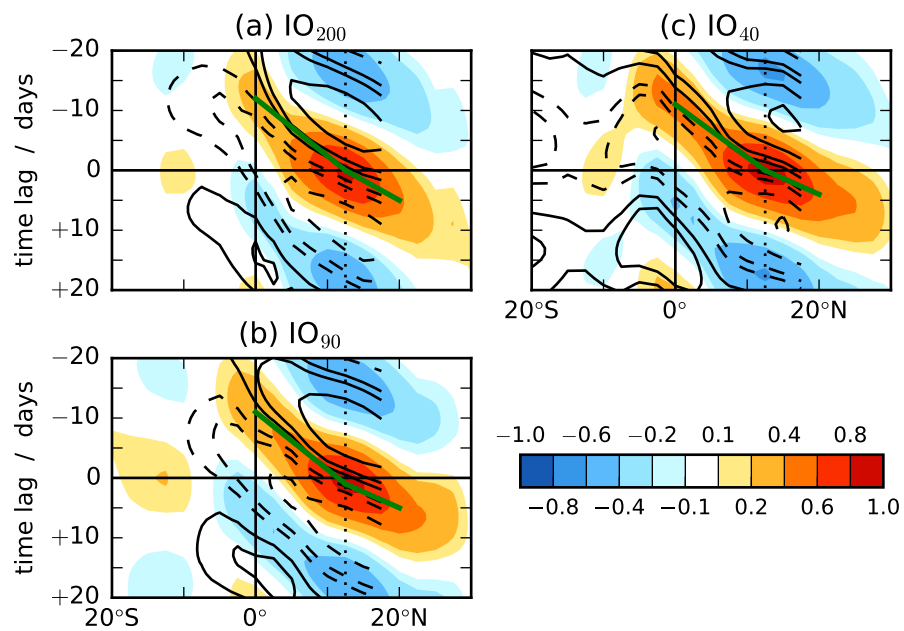
Figure 14. As figure 6 but for (a) IO$_{200}$, (b) IO$_{90}$ (repeat of figure 6e, for reference), (c) IO$_{40}$.
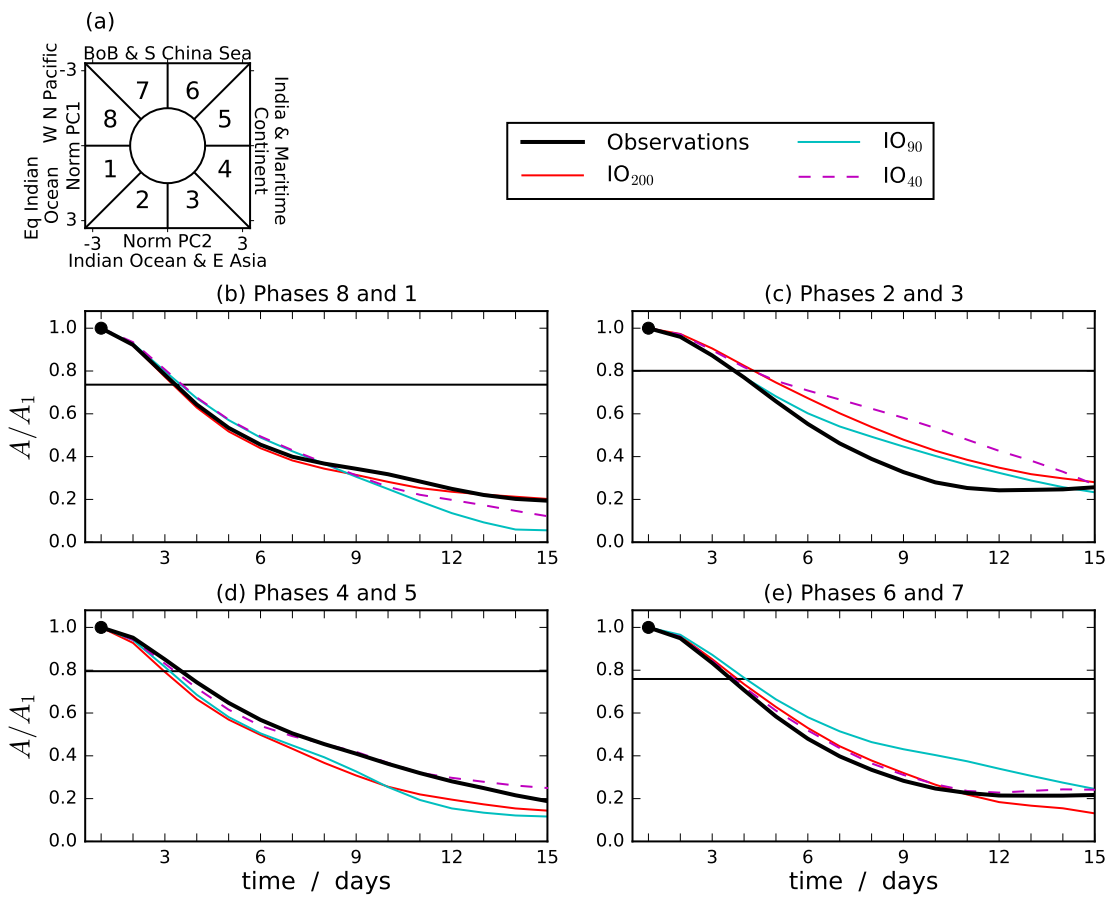
Figure 15. As figure 12 but for IO_{200}, IO_{90} and IO_{40}.